Tribology International 216 (2026) 111570

Contents lists available at ScienceDirect

Tribology International

journal homepage: www.elsevier.com/locate/triboint

Development of an embedded triboelectric rolling bearing for fault diagnosis and self-powered monitoring

Fangyang Dong [a,b,1], Peishuo Li [a,1], Zhixiang Chen [b,1], Guang-An Yu [a], Hengxu Du [a], Zhiying Zhang [a], Weilu Sha [a], Yiyang Huo [a], Taili Du [a,b,*], Minyi Xu [a,**]

[a] Dalian Key Lab of Marine Micro/Nano Energy and Self-Powered Systems, Marine Engineering College, Dalian Maritime University, Dalian 116026, China
[b] Collaborative Innovation Research Institute of Autonomous Ship, Dalian Maritime University, Dalian 116026, China

ARTICLE INFO

Keywords:
Smart bearing
Triboelectric effect
Fault diagnosis
Condition monitoring
Self-powering

ABSTRACT

Smart bearings aim to integrate sensors and processing units into conventional bearing structures to enable condition monitoring and fault detection. In this study, a compact and practical embedded triboelectric bearing (TE-bearing) is designed and implemented for monitoring and detection in an actual rolling element bearing, enabled by triboelectrification occurring between its rolling elements and raceways. First, the effects of the embedded structure on bearing strength and electrical output are analyzed through finite element simulations and experiments, determining an optimal design that balances structural stability and signal-to-noise ratio. Then, an effective signal processing method is proposed via the characteristics of the acquired current signals to extract fault features. Experimental results show that the proposed transducer can successfully detect local faults in bearings through clear fault signatures in the current signals, which match the bearing characteristic frequency bands. Subsequently, the extracted features are validated using three classic machine learning algorithms, achieving an average accuracy above 98 % in fault classification. Compared to a reference accelerometer, the triboelectric transducer outperforms in frequency domain analysis. Moreover, the time-series dataset also performs well on four popular deep learning models, all of which exceed 96 % classification accuracy. Ablation studies using raw current signals reveal that the proposed time shifting method significantly enhances the performance of lightweight models. Finally, a self-powered demonstration of real-time bearing temperature monitoring is presented. All implementations utilize solely a commercial deep groove ball bearing and two copper sheets, demonstrating great potential for practical application and further improvement.

1. Introduction

Smart bearings, which integrate or embed sensing devices into the bearing body, enable direct acquisition of service information at the source, offering a novel pathway for bearing condition monitoring [1]. Compared with traditional monitoring methods, smart bearings benefit from a higher signal-to-noise ratio (SNR) and faster responsiveness due to the proximity of their sensitive cells to the signal source. Early developments in smart bearing technology largely focused on sensor-on bearings, in which conventional bearings were modified with surface-mounted or grooved-in sensors to achieve self-sensing functionality. A representative example is SKF Insight technology, which integrates a radial sensing ring with sensors and wireless modules to enable real-time bearing condition monitoring [2]. Similarly, Schaeffler has introduced the VarioSense series, in which multiple sensing modules are flexibly configured and fixed on the inner ring to monitor various physical values as needed [3]. However, these designs inevitably introduce complex wiring, additional mass and volume, which may compromise the compactness of the original bearing. As smart bearing applications demand sensors with smaller size, enhanced functionality, and higher integration, recent advancements in sensor technologies have emphasized breakthroughs in intelligence, miniaturization, integration, and diversity. Meanwhile, since the power consumption of micro-sensors has dropped to the milliwatt or even microwatt level,

* Corresponding author at: Dalian Key Lab of Marine Micro/Nano Energy and Self-Powered Systems, Marine Engineering College, Dalian Maritime University, Dalian 116026, China.
** Corresponding author.
E-mail addresses: dutaili@dlmu.edu.cn (T. Du), xuminyi@dlmu.edu.cn (M. Xu).
[1] Contributed equally to this work.

https://doi.org/10.1016/j.triboint.2025.111570
Received 14 October 2025; Received in revised form 26 November 2025; Accepted 11 December 2025
Available online 16 December 2025

self-powering technologies have partially addressed the dependency of smart bearings on batteries [4]. To this end, scholars have explored the integration of sensing elements with relevant circuits, utilizing electromagnetic, piezoelectric, and triboelectric transduction mechanisms, to develop self-powered or self-sensing structural units for smart bearings. These autonomous units do not require external power sources to generate electrical signals, thereby further reducing the system weight and volume. Zhang et al. [5] proposed a circular Halbach electromagnetic rotational energy harvester for bearing condition monitoring, where the magnets and coils were installed in the cage and end cover respectively. Despite its notable advantages in stability and reliability, electromagnetic energy harvesting is not inherently designed for sensing and often entails a bulky physical space for structural and functional implementation. In contrast, piezoelectric and triboelectric technologies, when integrated with micro-electro-mechanical-systems (MEMS) technology on a millimeter scale, may be superior in preserving the structural integrity of bearings [4]. Zhang et al. [6] installed an arc-shaped piezoelectric sheet between the outer race of the rolling bearing and the bearing pedestal, which can not only supply power to sensors but also enable bearing fault detection. However, the alternating nature of the mechanical loads in the piezoelectric effect results in material aging, along with issues such as depolarization and charge leakage. Consequently, the service life and continuous monitoring performance of piezoelectric-based smart bearings are inherently limited by the lifespan of the piezoelectric material.

Triboelectrification is a common phenomenon and can be easily triggered and sustained by the repeated contact between friction surfaces inside bearings [7]. Triboelectric nanogenerators (TENGs), based on this effect, have been widely reported as promising self-powered sensing solutions [8], which studied for collecting mechanical energy from the environment to power sensors or directly transmit sensing information to Internet of Things (IoT) systems. Due to their intrinsic advantages of broad material choices, flexible structures, and fast response to motion, triboelectric technology has emerged as a competitive candidate for sensing elements in smart bearing systems. As a few examples, Han et al. [9] glued flexible electrodes to the outer ring of a rolling bearing to monitor localized faults. However, this design increases the bearing size and may cause high radial stress and electrode failure, as it is still in the prototype stage. Dong et al. [10] proposed using a triboelectric sensing layer on the outer raceway of the bearing to measure defects on rolling elements. Jiang et al. [11] and Gao et al. [12] created bearing end covers with thin-film electrodes attached, forming triboelectric pairs with the cage and rolling elements respectively to achieve bearing condition monitoring. But creating a friction surface inside the bearing and direct contact of the roller with the sensor could easily cause wear or spalling over time. In previous studies where the use of triboelectric sensors for bearing fault diagnosis within machine learning frameworks has been explored [10,13]. However, most of these efforts focused on end-to-end results, without explicitly identifying what features in the triboelectric signal are related to the faults. This study aims to design an embedded triboelectric transducer and addresses the above shortcomings.

In this study, a compact and practical triboelectric transducer was developed to monitor operating status and detect local faults in a commercially available ball bearing. The interdigitated copper electrodes are embedded into the outer ring of the standard bearing, which is the only structural modification, and directly interact with rolling elements and raceway to form a triboelectric generation unit. When the inner ring drives the rolling elements to rotate, the charged rolling balls, through friction with the raceway, will induce alternating charge flow between the electrodes to create measured electrical signals. The current signals are then utilized for bearing condition monitoring and local fault diagnosis. Three tests are conducted, including simulation, experimental measurements, and signal analysis, to test the performance of the embedded triboelectric bearing (TE-bearing). In the first test, the impact of the embedded structure on the bearing body and the electricity output of the TE-bearing are assessed. In the second test, a signal processing method is proposed for triboelectric signals, and the fault detection ability of the TE-bearing for a local fault on the cage, inner and outer races, and rolling element is comparatively investigated. In the third test, a self-powered sensing application of the TE-bearing is demonstrated. The results show that the proposed time shifting method effectively extracts fault features from the acquired triboelectric current signals, yielding clear fault signatures that match the theoretical bearing characteristic frequency bands. By applying various machine learning algorithms to these processed signals, bearing fault diagnosis can be achieved with classification accuracy exceeding 98 %, which outperforms the vibration signals used for comparison in this study. The time-series dataset also performs well on several deep learning models, all of which surpass 96 % accuracy, and ablation studies on raw current signals confirm that the proposed method significantly enhances the performance of lightweight models. Moreover, the electrical energy generated by the TE-bearing enables self-powered monitoring of bearing temperature in real time. The proposed TE-bearing demonstrates promising potential for application in smart bearings.

The structure of this paper is as follows: **Section 2** describes the structure design, measuring principle, finite element (FE) model, and electrical characteristics of the TE-bearing. **Section 3** introduces the signal processing method and the overall framework of this study. In **Section 4**, the experimental results of fault diagnosis and self-powered sensing are analyzed. Finally, the conclusion is presented in **Section 5**.

2. Design and manufacturing

2.1. Configuration and working principle

Fig. 1 illustrates the embedded structure of the designed TE-bearing. Without loss of generality, a standard KIF POM6310 deep groove ball bearing is employed as the bearing body, with the only addition being two groups of interdigitated copper electrodes. An explosive view of the components is shown in Fig. 1(a). It is well known that there is a compact layout for bearings, in which case the electrodes are fully embedded within the outer ring of the bearing. Only the lead terminals extend outward for signal output, as specifically demonstrated in Fig. 1 (a). To facilitate prototype manufacturing in this study, the polyoxymethylene (POM) outer ring was cut into two segments via laser machining, an outer shell and an inner shell, between which the electrodes were embedded. The remaining gaps were sealed and secured with insulating adhesive, and the assembled TE-bearing is shown in Fig. 1(b). The cage is made of reinforced nylon 66, providing good thermal resistance and self-lubrication, while both the inner and outer rings remain constructed from the original POM material. The bearing parameters are listed in Table 1.

The interdigitated electrode is laser-cut from a 0.2 mm thin copper sheet along the template depicted in Fig. 1(c). According to the diagram in Fig. 1(b), the length L of the electrode can be easily obtained as

$$L = \pi(d_m + D_b + 2d_1), \tag{1}$$

whose exact value is determined by the inner shell thickness d_1 varying with the embedding positions. The detailed is that the number of copper comb fingers each electrode has is equal to that of the rolling elements, $n_e = n_b = 13$, while two groups of electrode fingers keep alternately and evenly distributed in pair, as schemed in Fig. 1(c). This design ensures all elements leave and reach the same group of electrode fingers at the same time, thereby resulting in a stable and maximized output [14]. Here, each finger width l equals the spacing between two adjacent fingers, satisfying the relationship with the total length L given in Eq. (2),

$$l = \frac{L}{4n_e}. \tag{2}$$

In addition, the combined width of the interdigital electrode pairs

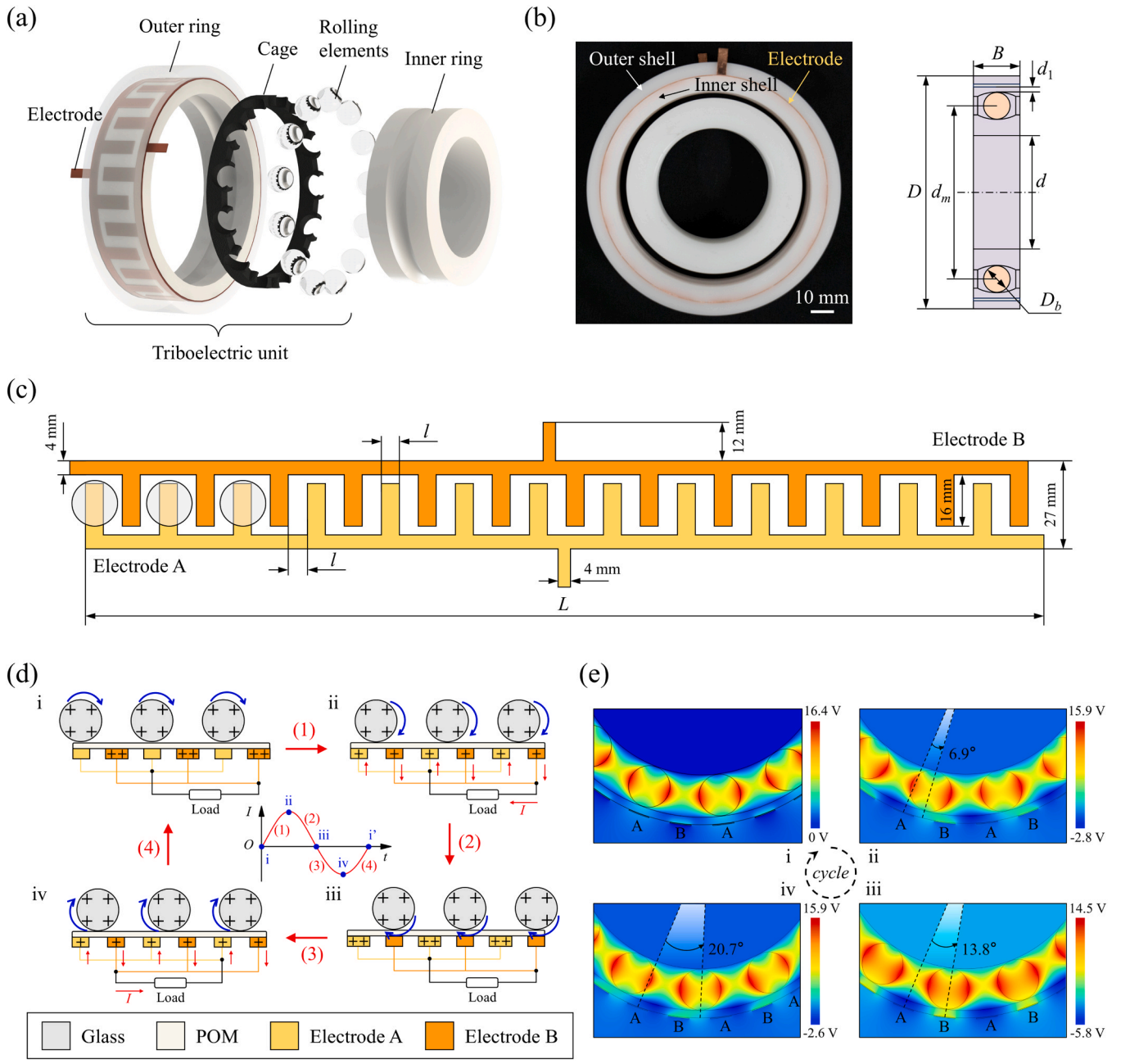

Fig. 1. Design of the TE-bearing. (a) Explosive view of the TE-bearing structure. (b) Photograph and geometry of the assembled TE-bearing. (c) Design of the interdigitated copper electrodes. (d) Triboelectrification mechanism in the TE-bearing, and (e) the corresponding electrostatic simulation results in FE analysis.

Table 1
Nomenclature of bearing dimension parameters.

Parameter	Symbol	Value (mm)
Pitch diameter	d_m	79
Rolling element diameter	D_b	11
Number of rolling elements	n_b	13
Contact angle (degree)	α	0
Outer diameter	D	110
Bore diameter	d	50
Width	B	27

equals to the bearing width B. Note here that each electrode finger measures 16 mm in length, and the sum of the width of their connecting band is greater than $1/2B$, ensuring they lie completely beneath the rolling elements for optimal charge induction.

It should be noted that this laser-cut, adhesive-sealed structure is adopted solely to complete the entire investigation, from structural design and mechanism validation to experimental testing, under laboratory manufacturing constraints. Compared with a commercial bearing, this prototype may exhibit reduced long-term durability, potentially influencing structural strength, dynamic performance, and fatigue life. These effects originate from the segmented POM outer ring and the presence of adhesive interfaces, which may alter load distribution or introduce minor stiffness discontinuities. Nevertheless, the goal of this study is to verify the feasibility and sensing mechanism of the embedded triboelectric transducer in bearing body. In future industrial manufacturing, the same embedded configuration can be realized through integrated injection molding or compression molding, allowing copper electrodes to be directly formed inside the outer ring. Such fabrication routes would eliminate the structural discontinuities of the

prototype and avoid potential long-term issues associated with laboratory processing, thereby ensuring the durability and service life required for practical smart bearing applications.

The contact electrification of the TE-bearing relies on coordination with other bearing components. The triboelectric unit, formed by the embedded outer race and the glass rolling elements, functions as a self-sensing structure capable of reflecting the operating state of the bearing. During typical operation, the inner ring rotates with the rotor, and the outer ring is fixed with the base. The cage evenly spaces the rolling elements and guides their smooth motion between the inner and outer rings. When driven by the rotor, the glass balls roll along the raceway of the outer ring and across the comb fingers of the interdigital electrodes, thereby generating alternating current (AC) for the external load. The principle of triboelectrification and charge transfer involved in this process is illustrated in Fig. 1(d). For ease of description and understanding, two groups of interdigitated electrodes are labeled as A and B, respectively. It is assumed that all glass balls are aligned with electrode A at the initial stage, isolated by the cage openings. After sufficient contact with the POM outer raceway, the glass balls tend to lose electrons and become positively charged [9], leaving behind net negative charges distributed on the surface of the raceway. When the glass balls are forced to roll toward electrode B (from Fig. 1(d) **i** to **iii**), due to the electrostatic induction, the potential between electrode A and B begins to change, driving electrons through the external circuit toward electrode B and resulting in a positive current peak. As shown in the inset, the points in the waveform correspond to these stages. Similarly, as the charged balls continue to roll, the induced positive charges on electrode A are driven back to electrode B, as displayed in Fig. 1(d) **iv**, until the electric potential restores to the initial state, producing a negative peak in the waveform. As the glass balls roll over multiple comb pairs of electrodes A and B, alternating positive and negative peaks appear sequentially in the time domain, which forms a continuous output waveform.

The above charge transfer process can be interpreted by the variance of electric potential across two electrodes in open circuit condition. As shown in Fig. 1(e), the potential distributions at four stages of a cycle are simulated by the FE method in the COMSOL Multiphysics. As the charges cannot transfer between electrodes without the load, the open-circuit voltage (V_{OC}) is defined as the electric potential difference between two electrodes [15]. For numerical calculation, a surface charge density of 8×10^{-6} C m^{-2} is assigned to the outer surface of the glass balls [16]. In the open circuit condition, two planar electrodes are both set the corresponding suspension potential and grounding. The quantifiable relationship of V_{OC} with the rotation angle of the glass balls can be obtained by subtracting the induced potentials on the two electrodes,

$$V_{OC} = V_B - V_A. \tag{3}$$

V_A and V_B are the induced potentials electrode A and B, respectively. The parametric sweep results (see Fig. A.1 of Appendix A) demonstrate the continuous variation of the V_{OC} with the rotation angle. Starting from electrode A, the simulated voltage signal behaves as a cosine waveform in the time domain. For the proposed TE-bearing, measurable electrical signals are generated periodically with the bearing rotation, serving as a critical foundation for condition monitoring.

2.2. Structural modeling

The redesign of bearings often involves grooving to accommodate embedded sensors, but the introduction of improper grooves may result in stress concentrations that have a negative impact on the strength and performance of the bearings [4]. To evaluate the embedded design inside the TE-bearing and simulate the structural response under load, a bearing FE model is adopted for further studies. Fig. 2(a) illustrates the FE models of the TE-bearing developed in ANSYS. The model includes the bearing inner ring, rolling elements, the outer ring integrated with the interdigitated electrodes, and a bearing housing, as shown in Fig. A.2. The cage is neglected in the simulation. The material properties of the FE model are presented in Table 2. The interaction between the rolling elements and the outer ring was defined as a frictional contact type. Bonded contact was used to simulate the embedded adhesive connection between the electrode and the outer ring. The model mesh consisted of a combination of coarse and fine elements. Basically, the target section for this simulation was the load zone of the bearing where maximum contact forces are applied to the outer ring. Therefore, a fine

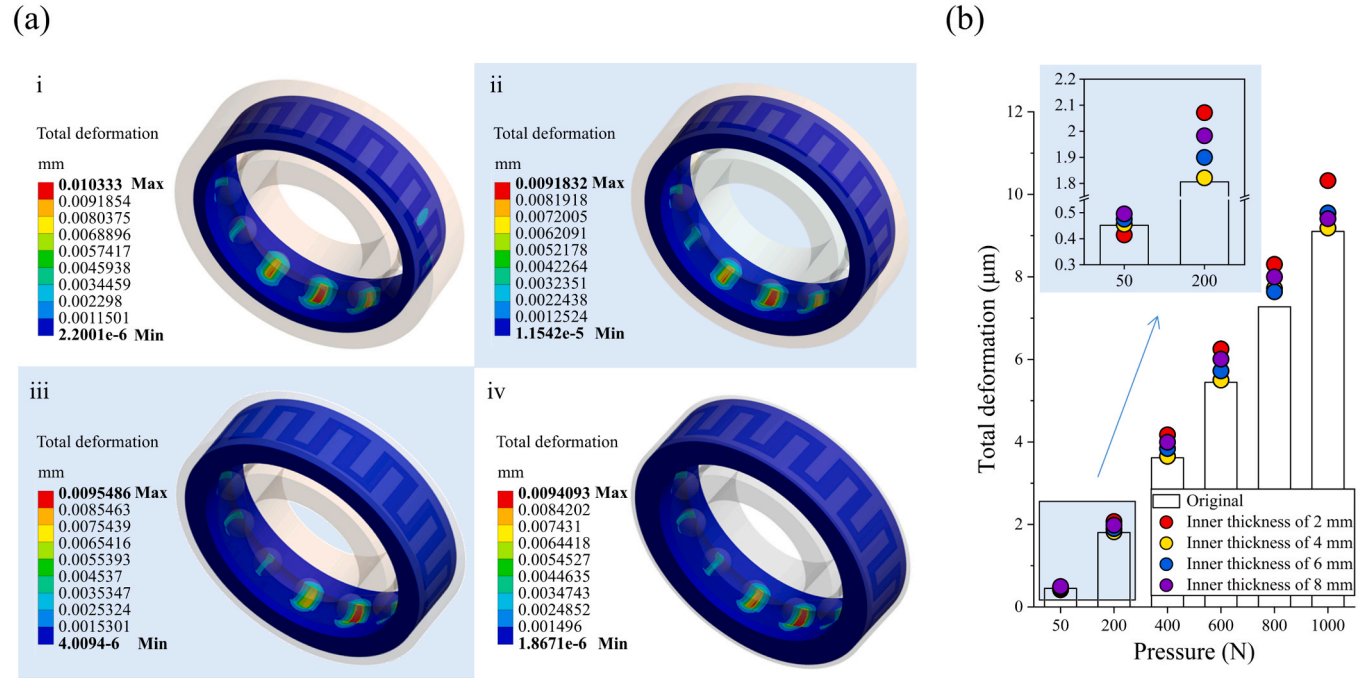

Fig. 2. Structural modeling of the TE-bearing. (a) Deformation contour of inner shells with different thicknesses under a 1000 N radial load. (b) Comparison of deformation for inner shells at each thickness under various radial loads.

Table 2
Physical properties of bearing materials in the FE model.

Material (component)	Young's modulus (GPa)	Poisson's ratio	Mass density (kg m^{-3})
POM (inner and outer ring)	2.6	0.39	1390
Glass (rolling elements)	68.9	0.23	2460
Copper (electrodes)	110	0.37	8900

mesh was applied to the contact zone between the rolling elements and the outer raceway, while the interdigitated electrode was meshed with three layers of linear elements across its thickness to capture bending deformation. As the bearing is subjected to radial loading only and no axial load is applied, the displacement of the inner ring nodes was constrained in the x-direction ($U_x = 0$) [17]. Due to having a thick steel made pedestal, it is assumed that the deformation of the pedestal is negligible. Hence, the displacement of the nodes at the bottom of the housing has been constrained ($U_z = 0$). A radial force in the -z direction was applied to the reference node on the inner ring bore surface to distribute the radial load.

During the rotation of the bearing, the load carried by each rolling element induces radial strain within the thickness of the outer ring. Considering the mechanical properties of the bearing materials used in this study, the applied loads in the FE calculation are restricted to within 1000 N to ensure that the structural deformation remains within a reasonable and practical operating range. Fig. A.2 illustrates the deformation of the outer ring in the original bearing under a radial load of 1000 N. For a moment when the elements are positioned exactly above the electrode fingers, the deformation contours of the embedded structure with varying inner shell thicknesses of 2, 4, 6, and 8 mm in the outer ring are presented in Fig. 2(a) i to iv, respectively. Under radial loading, the rolling elements come into contact with the outer raceway and induce deformation, which gradually increases from both sides toward the bottom. For example, in the case of a 4 mm inner shell thickness (Fig. 2(a) ii), the maximum deformation at the bottom of the outer ring reaches approximately 9.18 μm. A radially increasing load ranging from 50 to 1000 N is applied to the inner ring of the original bearing to investigate the deformation behavior of the outer ring under load, which is recorded as the baseline of 0.45, 1.81, 3.62, 5.44, 7.28, and 9.1 μm for comparison with the embedded design. As shown in Fig. 2(b), the deformation of the outer ring increases with the electrode embedding, across all applied radial loads. The outer rings with 4-, 6-, and 8-mm embedding depths exhibit deformation behaviors close to those of the original bearing. As the embedding depth decreases to 2 mm, the total deformation of the outer ring tends to increase. Fig. A.3 presents the deformation of the embedded outer ring when the rolling elements are located directly above the gap between comb fingers. As the inner shell thickness decreases and the radial load increases, the deformation of the outer ring becomes more pronounced. At a load of 1000 N, the maximum total deformation reaches 9.59 μm in the 4 mm case. In this study, it can be concluded that, with a suitable embedding depth, the adverse effect of the proposed electrode-embedded design on the structural strength of the bearing remains acceptable, pending further optimization for long-term applications. In addition, the current static loading analysis is conducted employing FE modeling to facilitate the feasibility investigation [18], while more accurate assessment of structural strength under dynamic conditions remains one of the future work objectives for this study.

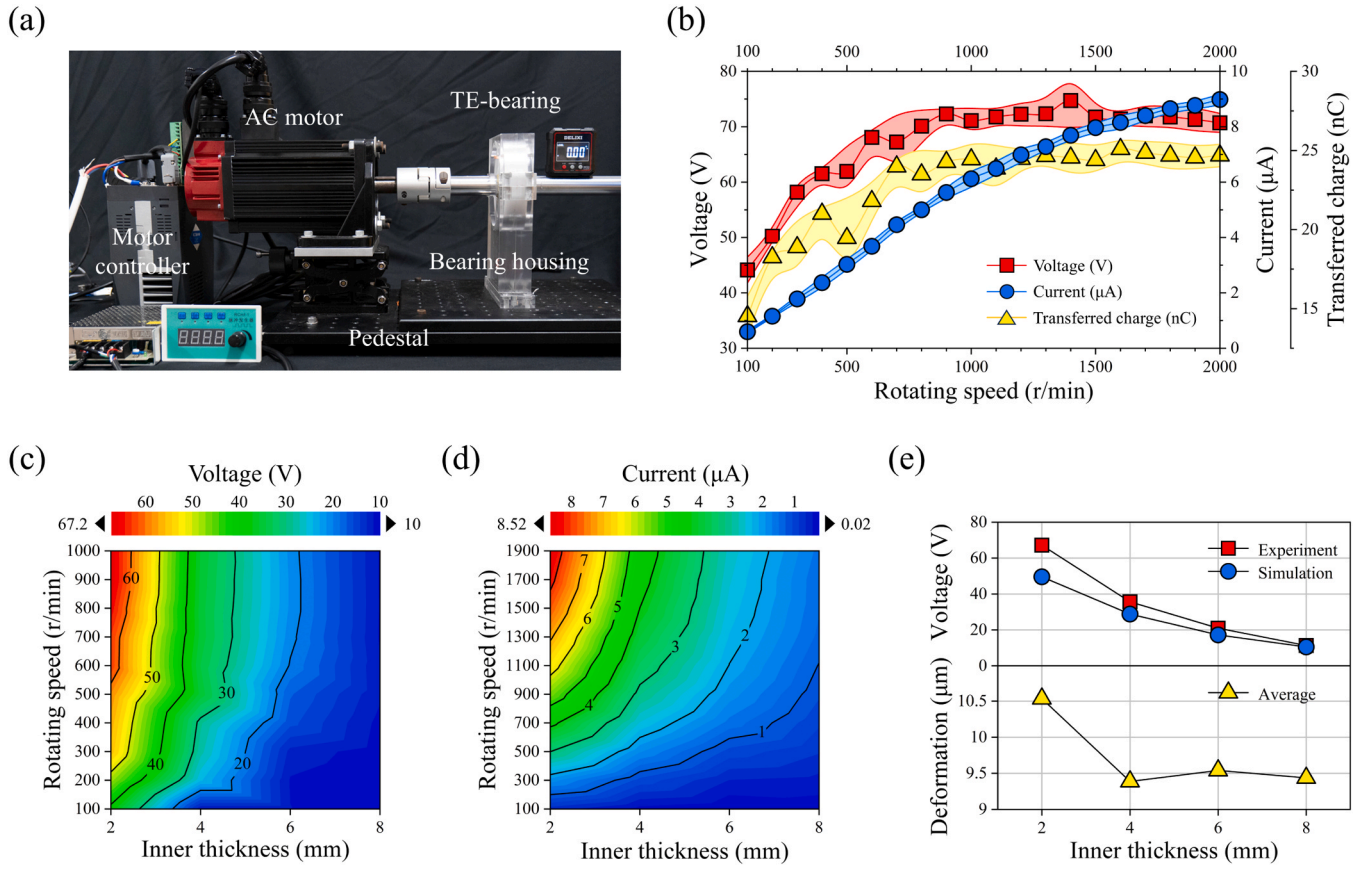

Fig. 3. Output characteristics of the TE-bearing. (a) Components of the bearing test rig. (b) Peak values of V_{OC}, I_{SC}, and Q_{SC} with varying rotor speed (inner shell thickness is 2 mm). (c) V_{OC} and (d) I_{SC} with different rotating speeds and inner shell thicknesses. (e) Experimental and simulated voltage amplitudes and outer ring deformations under different inner shell thicknesses.

2.3. Electrical output test

To validate its electrical output performance, a test bench for the TE-bearing supported rotor is constructed, as shown in Fig. 3(a). An AC servo motor drives the rotor at rotating speeds ranging from 0 to 3000 r/min, controlled by a frequency converter. The TE-bearing is secured via its housing and mounted on a pedestal. Electrical signals generated by the TE-bearing are transmitted through two wires connected to electrodes A and B, and are precisely measured using an electrometer (Keithley 6514) with a data acquisition (DAQ) module (NI 9215). The sampling frequency is set to 2 kHz. The signal waveform is also visualized in real time through a computer monitor during the experiment.

As illustrated in Fig. 3(b), the V_{OC}, short-circuit current (I_{SC}), and transferred charge quantity (Q_{SC}) of the TE-bearing with an inner shell thickness of 2 mm are measured at different rotating speeds. Notably, the mean peak value of I_{SC} increases almost linearly from 0.59 to 8.98 μA as the rotating speed increases from 100 to 2000 r/min. The V_{OC} and Q_{SC} of the TE-bearing show synchronized variation with increasing rotating speed. Their peak-to-peak values increase initially and then plateau at about 72 V and 42 nC, respectively, when the speed exceeds 600 r/min. V_{OC} is directly related to the constant transferred charges between the electrodes [19], whereas Q_{SC} depends on the surface charge density and the contact area. The initial low rotating speeds cannot guarantee the full contact. Once full contact is established, both V_{OC} and Q_{SC} stabilize and remain constant. Similar phenomenon is mentioned in Ref. [13]. The observed linear relationship between I_{SC} and speed can be interpreted through Eqs. (4) and (5) [7,19],

$$I_{SC} = \frac{dQ_{SC}}{dt} = \frac{dQ_{SC}}{d\theta}\frac{d\theta}{dt} = 2\pi\frac{dQ_{SC}}{d\theta}f_{cage}, \tag{4}$$

where $dQ_{SC}/d\theta$ represents the rate of change of electric charge, which serves as an inherent parameter in the fixed configuration of the TE-bearing. f_{cage} is the rotational frequency of the cage. Only considering the pure rolling, the relationship between f_{cage} and the rotating speed of the rotor can be expressed as

$$f_{cage} = \frac{1}{2}f_s\left(1 - \frac{D_b}{d_m}\cos\alpha\right). \tag{5}$$

f_s denotes the rotational frequency of the shaft representing the rotating speed. It can be observed that the short circuit current I_{SC} is linearly proportional to the rotor speed. Fig. A.4 presents the linearity with an R^2 value of 0.96 between I_{SC} and rotating speed, indicating an ability in bearing speed sensing.

The thickness of the inner shell of the outer ring, which functions as the dielectric layer, also affects the electrical output of the TE-bearing, as shown in Fig. 3(c) and (d). As the inner shell thickens, the V_{OC} and I_{SC} of the TE-bearing decrease significantly at all rotating speeds. At 600 r/min, the voltage plateaus of approximately 67 V, 35 V, 21 V, and 11 V are reached for inner shell thicknesses of 2, 4, 6, and 8 mm, respectively. Due to the plateaus, only the speed range below 1000 r/min is visualized in Fig. 3(c). As shown in Fig. 3(d), the I_{SC} remains sensitive to variations in rotating speed across different inner shell thicknesses, exhibiting an average linearity (R^2) of up to 0.95. Likewise, the current peak values decrease with increasing inner shell thickness, measuring 8.51 μA, 4.51 μA, 2.43 μA, and 1.38 μA at 1900 r/min, respectively. These behaviors can be explained by that the equivalent working mode of the TE-bearing corresponds to the attached-electrode type TENG, as investigated by Niu et al. [20]. When the inner race of the outer ring serves as the dielectric layer, both the inner shell thickness and the ball diameter are not negligible, where the short circuit transferred charges can be expressed as

$$Q_{SC} = \sigma S x\left[\frac{1}{x + \frac{d_1}{\varepsilon_{r1}}} + \frac{\frac{d_1}{\varepsilon_{r1}}}{\left(g + \frac{d_1}{\varepsilon_{r1}}\right)\left(g + \frac{d_1}{\varepsilon_{r1}} - x\right)}\right]. \tag{6}$$

Inside Eq. (6), σ, S, x, g are the initial surface charge density on the dielectric layer, the contact area size between the rolling element and the inner race, the separation distance, and the total gap thickness between two electrodes, respectively. The effective dielectric thickness is defined as the inner shell thickness d_1 divided by its relative dielectric constant ε_{r1}, $\delta_1 = d_1/\varepsilon_{r1}$. While $x = g$, the rolling ball reaches the next electrode, the total short-circuit charges will be transferred. Thus, Eq. (6) can be further simplified to

$$Q_{SC} = \frac{2\sigma S x}{g + \delta_1}, \tag{7}$$

where Q_{SC} decreases with the increase in inner shell thickness d_1, leading to a reduction in I_{SC} as indicated by $I_{SC} = dQ_{SC}/dt$. From the basic equation between V_{OC}, Q_{SC} and C [21], the open circuit voltage can be obtained as

$$V_{OC} = \frac{2\sigma x}{\varepsilon_0}\frac{\delta_1\delta_2}{{\delta_1}^2 + g(\delta_1 + \delta_2) + 2\delta_1\delta_2}. \tag{8}$$

ε_0 is the vacuum permittivity, and δ_2 represents the effective dielectric thickness of the rolling ball, both of which remain constant. Therefore, V_{OC} also tends to decrease with increasing dielectric thickness. In addition, a thinner dielectric film has been reported to be favorable for enhancing the surface charge density σ [22,23].

To directly compare with the experimentally and numerically obtained voltage values, Fig. 3(e) presents the average deformation of the outer ring under varying inner shell thicknesses at a radial load of 1000 N. Here, the average deformation is defined as the arithmetic mean of the outer ring deformation when the rolling elements are located above the electrode fingers and the gap between electrodes (as shown in Fig. 2(a) and Fig. A.3). The outer ring sustains a relatively large deformation of 10.54 μm when the inner shell thickness is 2 mm. As the thickness increases beyond 4 mm, the average deformation of the outer ring significantly decreases and stabilizes to close values of 9.39 μm, 9.54 μm, and 9.44 μm, respectively. Compared with the original bearing deformation of 9.1 μm, the structural strength degradation introduced by the TE-bearing modification is confined within the micrometer scale. Considering the electrical sensitivity discussed above, a 4 mm inner shell thickness of the outer ring is adopted as the optimal configuration for the TE-bearing in this study.

Moreover, it is noted that the simulated V_{OC} follows a trend consistent with the experimental results, yet its overall magnitude is lower. This is mainly because the electrostatic field module in COMSOL cannot capture the contact and deformation between the rolling elements and raceways induced by centrifugal forces. The deviation observed at a thickness of 2 mm further supports that a thinner shell results in greater deformation, thereby improving interaction and contact. The detailed simulation results can be found in Fig. A.1, which illustrates how the simulated V_{OC} varies with the rolling element rotation for various shell thicknesses.

3. Methodology

3.1. Issue description and framework summary

In addition to the general advantages of the embedded triboelectric-based method, such as low-cost and lightweight integration, non-contact measurement independent of mechanical force or deformation, and fast response with a high SNR, the close proximity to the core rotor area enables more suitable monitoring of certain fault conditions. The main problems surrounding the vibration analysis of bearings are the

smearing effect of signal transfer path and the background noise [24]. By installing the sensor on the housing, impulses generated by defects travel through multiple paths to reach the transducer. Compared to the overall vibration of the system and noises from surrounding components or machines, the defect-induced impacts with low energy become weaker. Signals from various components further lose their energy on the path to reach the sensor due to structural damping and long transmission path, and may not be detectable [17]. Furthermore, in rolling element bearing degradation assessment based on vibration signal, a universal set of equations can be used to calculate bearing characteristic frequencies (BCFs) to reveal the location of a fault and its severity [25]. BCFs calculation of varying types can be performed using the methods outlined in [17,26], as listed in Table 3. There is no such set for triboelectric-based bearings, and whether BCFs are applicable is yet to be verified. Therefore, another objective of this study is to develop a methodology based on triboelectric signals for general conclusions or applications, that is, it explores fault features in the frequency domain, constructs a fault model, and complements the lack of interpretability in using machine learning techniques.

Aiming to address the problems of bearing fault diagnosis based on triboelectric signals, this study proposes a concise and logical framework to simplifying the process of fault signals from collection and processing to identification. Fig. 4(a) summarizes the overall flow of the proposed architecture:

(1) The short-circuit current of the TE-bearing is acquired using the electrometer and DAQ module, and saved as the raw current signal.
(2) The acquired raw current signal is delayed by half a period in the time domain to obtain the delayed current signal. Subsequently, the raw and delayed signals are added to derive the current residuals.
(3) The residual signals obtained from different operating conditions, i.e., various bearing fault types, are labeled and segmented into time windows of appropriate length to form a sequential dataset.
(4) Envelope spectrum analysis is applied to the residual segments to extract frequency features, resulting in the creation of a frequency-domain dataset.
(5) Each dataset is divided into the corresponding training set, validation set, and test set. Various machine learning models are trained using the training and validation sets, and the best performing model is retained. Finally, the test set is used to evaluate the classification performance for further analysis.

3.2. Time shifting

When there is a local fault on one raceway of the bearing, passing rolling elements over the local fault creates pulses at one of the fundamental BCFs [25]. In this study, we consider that a slight contact loss or impact occurs when a rolling element is in contact with a damaged area (e.g., outer race crack), resulting in a transient velocity fluctuation. These fluctuations may directly alter the relative slip rate, contact area, and contact force between the rolling element and the raceway [7,27]. Each time rolling elements traverse the defect, the resulting impacts or disturbances also occur periodically, exhibiting constant frequency components in the frequency domain. Apart from the previously highlighted sensitivity of the I_{SC} to rotational variations, the governing equation for the current, which is its relationship with the velocity of rolling elements, can be expressed as

$$I_{SC} = \frac{dQ_{SC}}{dt} = \frac{dQ_{SC}}{dx} v = \frac{2\sigma S v}{g + \delta_1}. \tag{9}$$

Therefore, the short-circuit current can serve as a reliable indicator for bearing fault information.

In the event of a single-point bearing defect in the TE-bearing, the expression for its triboelectric current signal should be represented as

$$I(t) = I_0 \sin\left(\omega t\right) + \sum_{n=-\infty}^{\infty} [A_n \delta(t - nT_c)] + N(t), \tag{10}$$

where first term denotes the baseline sinusoidal AC signal in normal condition, the second term is represented a periodic impulse sequence to model the fault disturbance, and $N(t)$ represents the Gaussian background noise. In conjunction with Eq. (10), reducing or eliminating the periodic current signal components is essential for enhancing the fault-related features. Considering a steady-state condition in which impacts occur periodically (T_c), the impulse amplitude A_n can be treated as a constant value A. $I_{imp}(t)$ is rewritten to

$$I_{imp}(t) = A \sum_{n=-\infty}^{\infty} \delta\left(t - \frac{n}{f_c}\right), \tag{11}$$

which admits the Fourier expansion:

$$I_{imp}(t) = Af_c + 2Af_c \sum_{n=1}^{\infty} \cos(2\pi f_c n t). \tag{12}$$

Currently, given that the magnitude of Af_c is much small than that of current I_0, the current signal $I(t)$ is approximated as

$$I(t) = I_0 \sin(\omega t) + 2Af_c \sum_{n=1}^{\infty} \cos(n\omega_c t) + N(t). \tag{13}$$

The modulation coefficient β_n is defined as $\beta_n = 2Af_c/I_0$, where β_n is much smaller than 1. Except for the noise, the phase current suffering from bearing fault can be modulated as

$$I(t) \approx I_0 \left[1 + \sum_{n=1}^{\infty} \beta_n \cdot \cos(n\omega_c t)\right] \sin\left(\omega t\right), \tag{14}$$

where ω and ω_c are the angular momentum representation of current and fault frequencies. To clearly reveal the effect of the fault in the frequency domain, Eq. (14) is transformed into

$$I(t) = I_0 \sin\left(\omega t\right) + \frac{I_0}{2} \sum_{n=1}^{\infty} \beta_n [\sin((\omega + n\omega_c)t) + \sin((\omega - n\omega_c)t)]. \tag{15}$$

By delaying the signal by half a period, the resulting delayed current is given as follows,

$$I\left(t - \frac{\pi}{\omega}\right) = I_0 \sin\left(\omega\left(t - \frac{\pi}{\omega}\right)\right) + \frac{I_0}{2} \sum_{n=1}^{\infty} \beta_n \left[\sin\left(\left(\omega + n\omega_c\right)\left(t - \frac{\pi}{\omega}\right)\right) + \sin\left(\left(\omega - n\omega_c\right)\left(t - \frac{\pi}{\omega}\right)\right)\right]. \tag{16}$$

Adding the delayed signal to the raw signal, the current residual is calculated as

Table 3
Bearing characteristic frequencies.

Description	Formula	Fault location
Ball pass frequency on outer race (BPFO)	$\frac{nf_s}{2}\left(1 - \frac{D_b}{d_m}\cos\alpha\right)$	Outer ring
Ball pass frequency on inner race (BPFI)	$\frac{nf_s}{2}\left(1 + \frac{D_b}{d_m}\cos\alpha\right)$	Inner ring
Ball spin frequency (BSF)	$\frac{f_s d_m}{D_b}\left(1 - \frac{D_b^2}{d_m^2}\cos^2\alpha\right)$	Rolling element
Fundamental train frequency (FTF)	$\frac{f_s}{2}\left(1 - \frac{D_b}{d_m}\cos\alpha\right)$	Cage

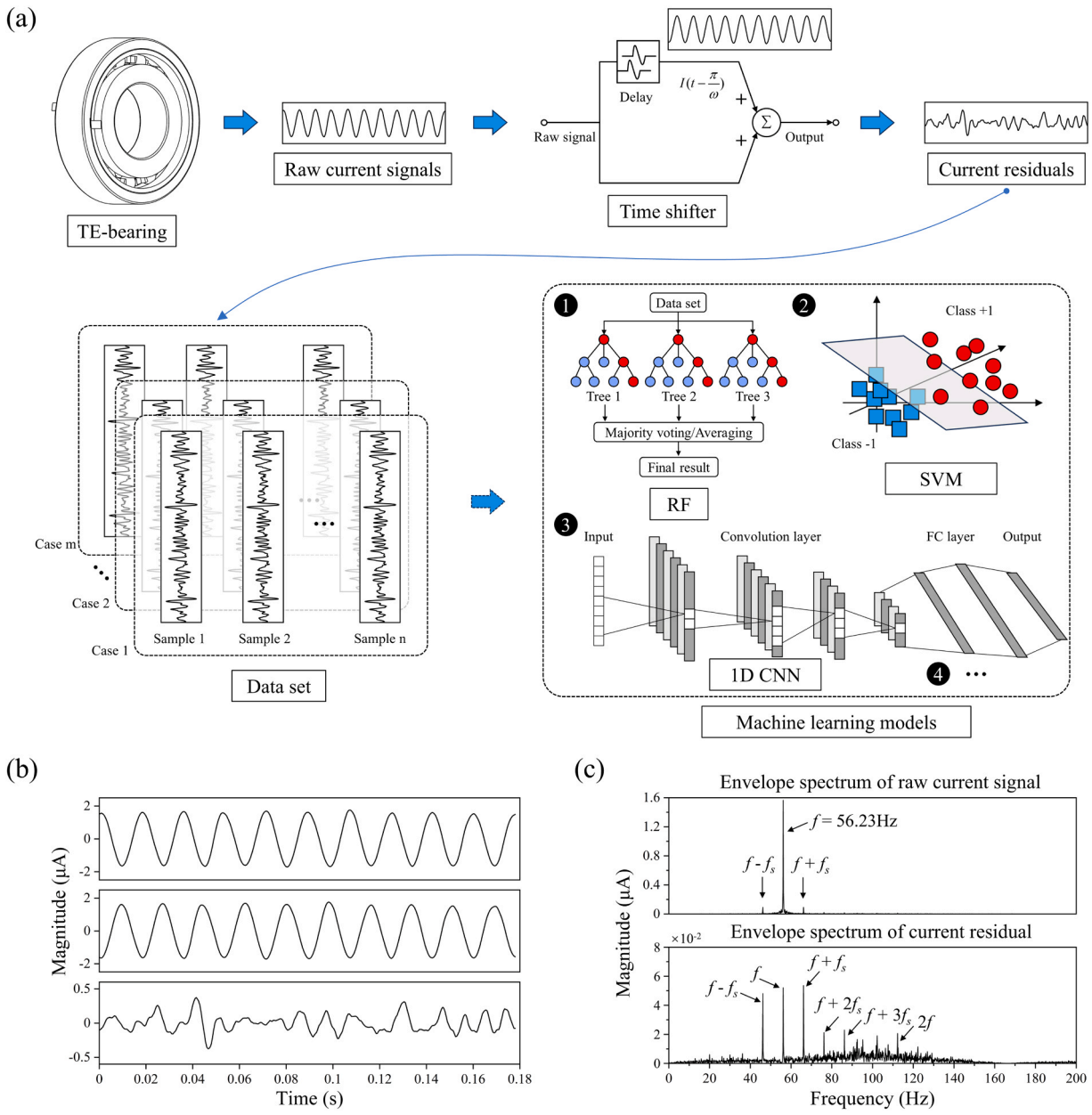

Fig. 4. Establishment of data sets. (a) Frame of the proposed method. (b) Time shifting in a current signal under a motor speed of 600 r/min and (c) its envelope spectrum.

$$I_{res}(t) = I(t) + I\left(t - \frac{\pi}{\omega}\right) = \frac{I_0}{2}\sum_{n=1}^{\infty}\beta_n\left[I_F(t) + I_F\left(t - \frac{\pi}{\omega}\right)\right]. \tag{17}$$

As a result, the fundamental component of the current signal is eliminated. The remaining fault component is represented by $I_F(t)$. Accordingly, the fault appears as certain frequency components as $f \pm nf_c$.

In the case of the motor at 600 r/min, Fig. 4(b) illustrates the implementation of time shifting in a current signal with a fundamental frequency of 56.23 Hz. Here, the dominant response of the triboelectric signal is a quasi-sinusoidal waveform generated by the continuous rotation of the rolling elements across the electrodes, which contributes the major amplitude. Thus, the fundamental frequency represents the frequency of the triboelectric current f. According to the principle in Fig. 1(c), a waveform is generated, once the rolling elements driven by the cage pass a pair of electrode fingers. Thus, the frequency of the current signal can be quantified as

$$f = n_e f_{cage}, \tag{18}$$

where n_e denotes the pair number of electrode fingers and satisfies $n_e = n_b = 13$ in the design. Substituting the corresponding dimensions from Fig. 2(c) into Eq. (5), the cage frequency at the rotor speed of 600 r/min can be calculated as $f_{cage} = 0.4325 \times f_s = 4.33$Hz. The calculated fundamental frequency is $f = 13 \times f_{cage} = 56.23$Hz. In this implementation, the raw current signal is added to its delayed signal, resulting in the current residual as shown in Fig. 4(b). Fig. 4(c) presents the envelope spectra of both the raw current and the current residual signals. The comparison between them demonstrates the effectiveness of the time shifting method in eliminating the fundamental component and highlighting other features.

4. Experimental validation

To verify the feasibility, accuracy, and simplicity of the proposed

method, two groups of experimental data are employed for analysis in this study, triboelectric current signals and vibration acceleration signals which used as a reference. Both data are obtained through comprehensive measurements of reliable test benches and data acquisition equipment, enabling thorough analysis of the operation under different fault conditions.

4.1. Fault diagnosis experiments on current residuals data

4.1.1. Data collection

The customized platform shown in Fig. 3(a) is further designed and utilized to collect authentic current signals under various operating conditions. Examples of single-point defects are cracks, pits or holes, and spalls [25]. In the destructive tests of this study, structural defects were manually introduced into the cage, inner raceway, outer raceway, and rolling elements of the TE-bearing using drilling and milling techniques [28,29], resulting in four types of bearing faults as illustrated in Fig. 5. The currents generated by the TE-bearing were acquired via the electrometer connected to a DAQ module, with a sampling frequency of 2 kHz. An ordinary performance computer (CPU: Intel i5–10400F 3.60 GHz; GPU: NVIDIA GeForce GTX 1050Ti) was employed for further subsequent data processing procedures, after which the data will be saved for diagnostic analysis.

It is worth noting that this study does not aim to establish a comprehensive database for bearing fault diagnosis based on triboelectric signals, but obtaining a relatively simplified and interpretable categorization scheme. Typical types of bearing faults are included in the datasets used in this study. As shown in Table 4, the current residuals data comprise five categories: a normal state, cage fault state, inner race fault state, outer race fault state, and ball fault state. A fracture was manually induced into the cage. For both inner and outer race faults, the hole diameter of the drilled damage was 3 mm. The localized defect

Table 4
Categorization and extent of bearing damage.

No.	Condition	Size (mm)
0	Normal	/
1	Crack on cage	/
2	Drilling on inner race	3
3	Drilling on outer race	3
4	Milling on a ball	0.5

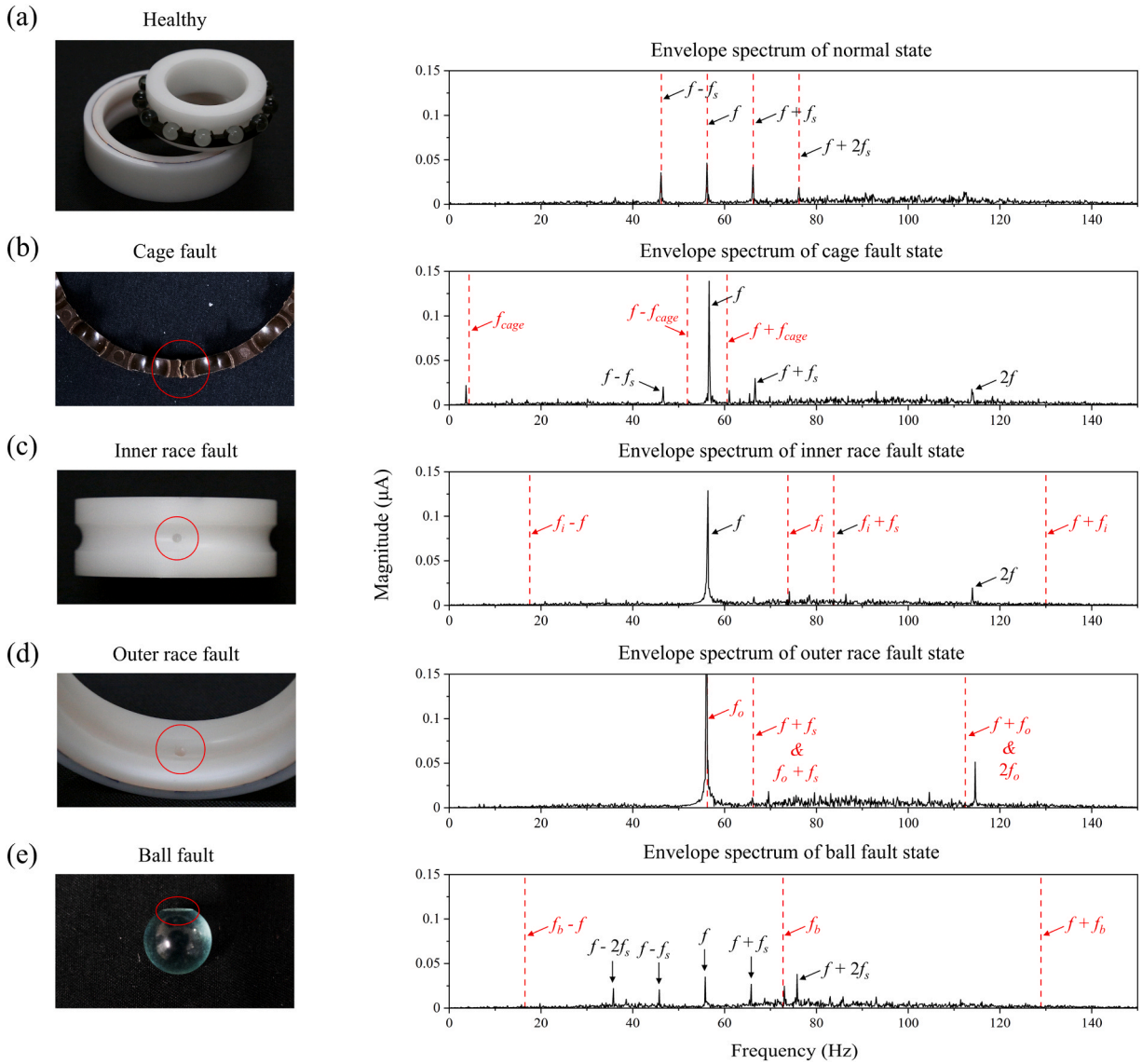

Fig. 5. Analysis of envelope spectrum of the current residuals in various operating conditions: (a) normal, (b) cage fault, (c) inner race fault, (d) outer race fault, and (e) ball fault.

measuring 0.5 mm in depth and 3 mm in diameter was created on the rolling element.

4.1.2. Envelope spectrum analysis

In theoretical analysis, bearing faults are assumed to introduce periodic pulse fault signals into the triboelectric current signals. Since no established calculation method currently exists for diagnosing bearing faults based on triboelectric signals, the use of conventional BCFs formulas (as shown in Table 2) is adopted to calculate the fault frequencies of the TE bearing. The involved bearing parameters are listed in Table 1. Based on the geometry size and the present speed, the bearing fault frequency for an outer race defect should appear at $BFPO = 56.23$Hz, and $f_i = 73.78$ Hz for an inner race defect. Table 5 summarizes the values of these characteristic frequencies. It is expected to capture these frequencies according to the location of the local faults.

Fig. 5 presents the envelope spectrum of the residual signals of the experimental current at five bearing states, which have undergone time shifting and low-pass filtering denoise processing. The locations of frequency features have been indicated by red lines. As found in Fig. 5(a), the low frequency domain from 0 to 150 Hz exhibits four distinct characteristic frequency components, denoted as 46.14 Hz, 56.15 Hz, 66.16 Hz, and 76.17 Hz, respectively. Since the current residual amplitude in the normal condition is modulated by the BPFO, the frequency domain of the normal signal obtained by the envelope spectrum mainly contains low magnitude BPFO (or $f_o = f = 56.23$Hz) and its harmonics ($f - f_s = 46.23$Hz, $f + f_s = 66.23$Hz, and $f + 2f_s = 76.23$Hz). In the faulty conditions as shown in Fig. 5(b), (c), and (d), the magnitudes of the BPFO and its harmonics in the envelope spectrum increase significantly compared to the normal state. A significant amplitude elevation in 3.66 Hz, 52.24 Hz, and 61.03 Hz differed from other states, corresponding to the FTF ($f_{cage} = 4.33$Hz) and its harmonics ($f - f_{cage} = 51.91$Hz and $f + f_{cage} = 60.56$Hz), appears in the envelope spectrum of cage fault state (Fig. 5(b)). The inner race defect signatures are marked by red lines in Fig. 5(c), where the findings of 74.09 Hz and 86.42 Hz aligns with the BPFI (or $f_i = 73.78$Hz) and its harmonics ($f_i + f_s = 83.78$Hz). Due to the relatively high detectability of the artificial outer ring faults, the magnitudes at the BPFO (56.23 Hz) and its harmonics ($f + f_o = 2f_o = 112.46$Hz) shown in Fig. 5(d) exhibit a significant increase compared to those in the normal state and even other fault types. Given the presence of a relatively modest inherent load in the drive system, fault frequencies could undergo slight displacement in frequency domain [28]. Fig. 5(e) demonstrates the envelope spectrum of current residual signal in case of a local fault on one of the rolling elements (balls). The BSF ($f_b = 70.42$Hz) is elevated by a faulty ball in the frequency spectrum, which may indicate superior fault feature visibility compared to previous report using piezoelectric sensor [17]. Moreover, the local fault on the rolling elements can affect both the inner and outer raceways, resulting in frequencies modulated by either BPFO or BPFI [30]. This explains the appearance of amplitude modulation at BPFO and its harmonics, i.e., f and $f \pm f_s$. Therefore, it can be concluded that (1) the TE-bearing is capable of detecting bearing faults at different locations, (2) the fault features are located at $f \pm nf_c$, where the fundamental frequency of current signals f varies with the rotating speed, and (3) the fault frequencies f_c still follows the universal equation set of BCFs. They provide a compelling basis for employing machine learning in the subsequent fault analysis.

It is worth noting that many harmonics present in the raw current are not considered in this section, but rather the primary focus lies on the fundamental component and its harmonics. Following the proposed time shifting strategy, these harmonics have been significantly attenuated, resulting in relatively clean frequency domains and features, which are favorable for subsequent analysis within learning models. Most of the remaining harmonics, especially the odd ones, undergo phase shifts and persist in the residual current, potentially contributing to the fault characteristics. Further investigation aimed at comprehensively analyzing the behavior of each individual harmonic in the current is considered worthwhile.

Table 5
Bearing fault frequencies.

Rotating speed (r/min)	BPFO or f_o (Hz)	BPFI or f_i (Hz)	BSF or f_b (Hz)	FTF or f_{cage} (Hz)
600	56.23	73.78	70.42	4.33

4.1.3. Data pre-training processing and performance

Further data mining is performed using a one-dimensional convolutional neural network (1D-CNN) to identify the fault patterns hidden in the triboelectric current signals. With the big volume of data, selecting samples of appropriate lengths is essential for effective deep learning. Due to the evident periodicity of current signals (rotating speed of 600 r/min), a sliding window (SW) has been adopted in this study. The width of the SW is set to accommodate these samples for putting into CNN and other subsequent models. Here, the sampling frequency is 2 kHz, and each condition is recorded for over 2 min, resulting in approximately 210000 data points per condition (denoted as l). Given that after the fast Fourier transforming the residual signal from the time domain to the frequency domain, as shown in Fig. 6(a), the size of each sample will be reduced to $2048/2 = 1024$. The effective frequency range of interest of 0–200 Hz determined by Fig. 5, contains 1024 points, i.e., the size of each frequency-domain sample is 1024. As a result, the window width d_1 is set to $1024 \times 2 \times 5 = 10240$, where the factor of 2 originates from the Nyquist relation and the multiplier of 5 ensures that each sample contains several rotation cycles for stable feature extraction. The stride d_2 depends on the input data size (2048 units in this case). The number of frequency-domain segments can be obtained as 97 using Eq. (19):

$$n = \frac{l - d_1}{d_2}. \tag{19}$$

Therefore, the frequency-domain segments are collectively organized into a data structure of size (485, 1024, 1) for model training.

The visual architecture of the CNN employed in the experiments is illustrated in Fig. 6(b). The input layer allows a shape corresponding to each individual segment of (1024, 1). The network comprises three convolutional blocks, each of which shares a similar structure, consisting of a 1D convolution unit, a rectified linear unit (ReLU) activation, and a maximum pooling (Max-pooling) layer. The number of input and output channels varies across layers, while other parameters are provided in Table 6. A dropout unit is applied as a regularization strategy to mitigate overfitting. Two fully connected layers are employed to transform the extracted features, which are then fed into a classifier to obtain the final prediction results. To facilitate model development and evaluation, the processed segments are randomly shuffled within each class and then split using a 6:2:2 ratio, with 60 % used for training the model, 20 % for validating and tuning hyperparameters during the training process, and the remaining 20 % employed as test set to report the final performance metrics. Besides, the Adam optimizer is utilized to conduct the back propagation, and the mean squared error (MSE) is adopted as the loss function. The training is performed with a batch size of 16 and an initial learning rate of 2×10^{-4}. Fig. 6(c) depicts the accuracy and loss curves for training and validation sets to visualize the network training process. By training 20 epochs, the oscillation amplitude of accuracy curves has reduced to less than 10 %, and after epoch 30, both accuracy and loss curves flatten out (as shown in the inset), indicating that the model has converged and generalized enough to avoid overfitting. As no further performance improvement is observed beyond it, the training epochs are set as 50 to balance model quality and computational cost. The network converging rapidly during training highlights the advantage of the triboelectric dataset in providing distinctive feature representations for learning [7]. Intuitively, the fully connected layer is visualized using the t-distributed Stochastic Neighbor Embedding

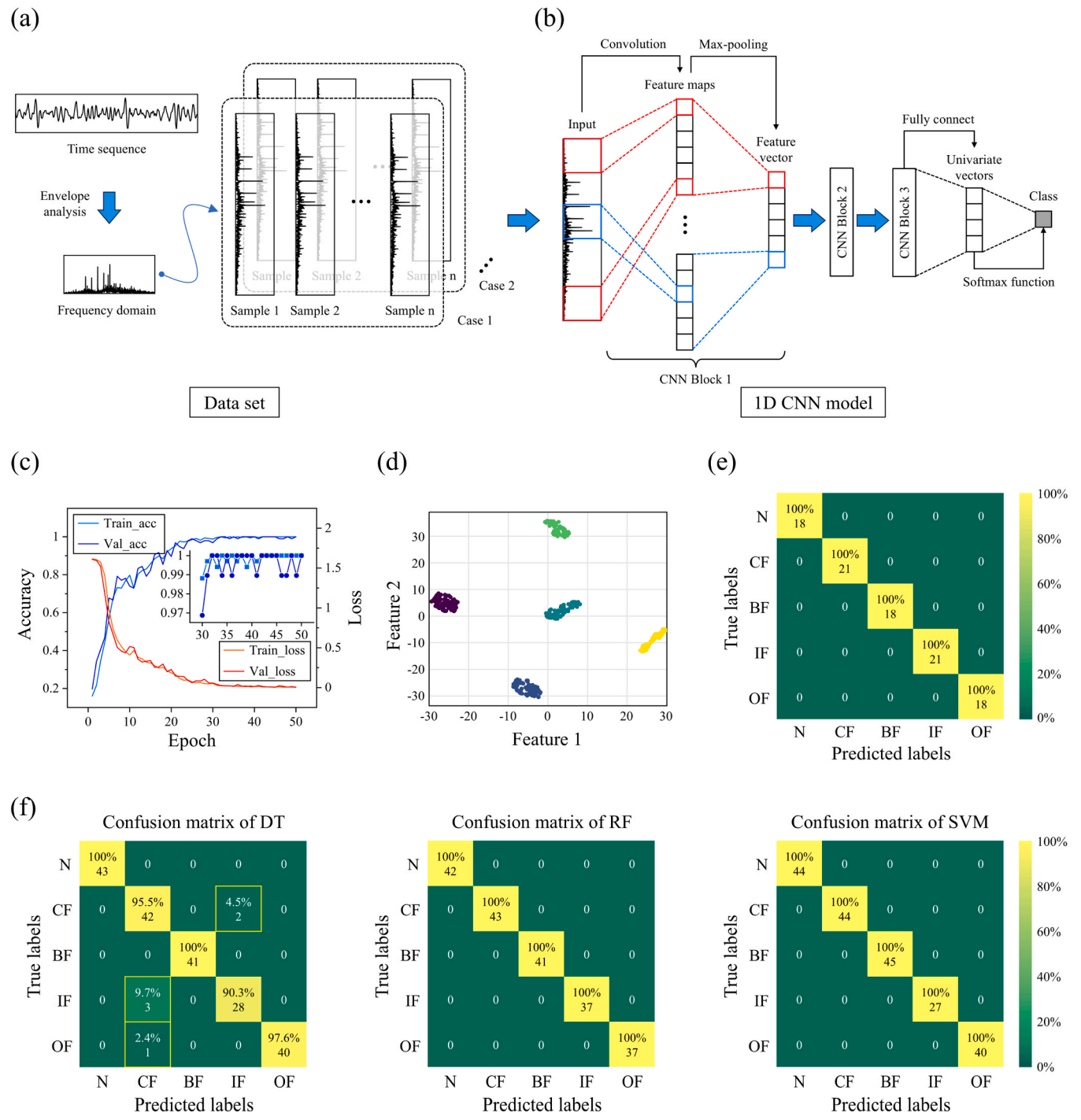

Fig. 6. Results of the proposed network and machine learning methods for Current residuals Data. (a) Construction of the frequency-domain dataset. (b) Structure of the three-layer convolutional neural network. (c) Accuracy and loss curves during training. (d) Feature visualization of the penultimate layer using the t-SNE analysis. (e) Confusion matrix the classification results for the five bearing conditions. (f) Confusion matrices of three machine learning classification models: DT, RF and SVM.

(t-SNE) algorithm [31], which reduces the abstract features from high-dimensional space to two dimensions, with samples of the same label plotted in the same color. As shown in Fig. 6(d), the test samples exhibit clear clustering, with the points of the same color tightly grouped and kept a long distance from others, implying that the model can fully mine the abstract features across different labels. Fig. 6(e) presents the confusion matrix of the classification results on the test set for five different states. All 96 test samples are correctly classified. Furthermore, the samples are re-divided and the model is repeatedly trained and tested 5 times to reduce the randomness inherent in both data splitting and deep learning. The results are shown in Table 7. In one of the diagnostic runs, 22.7 % of the inner race fault samples are misclassified by the CNN as outer race fault states. In this study, it may be attributed to the visual similarity observed in the frequency spectrum, as shown in Fig. 5(c) and (d). The diagnostics for faults located on the inner race of the bearing has long been a recognized challenge [28]. Even so, the average diagnosis accuracy of the proposed CNN model reaches 98.1 %, and no faults are misclassified as healthy states.

To demonstrate the necessity of each step in the proposed methodology, ablation experiments are conducted by selectively excluding

Table 6
Hyperparameter settings of the convolutional neural network.

Input data (1024, 1)	
Convolutional layer 1	Input channels: 1, Output channels: 32, Kernel size: 7 ReLU Max-pooling, Filter size: 2 Output size (512, 32)
Convolutional layer 2	Input channels: 32, Output channels: 64, Kernel size: 5 ReLU Max-pooling, Filter size: 2 Output size (256, 64)
Convolutional layer 3	Input channels: 64, Output channels: 128, Kernel size: 3 ReLU Max-pooling, Filter size: 2 Output size (128, 128)
Adaptive Avg-Pooling	Output size (128, 9)
Fully connected layer 1	Input channels: 1152, Output channels: 500 ReLU Dropout, p = 0.5
Fully connected layer 2	Input channels: 500, Output channels: 5 ReLU
Final output (input size: 5, classified by softmax)	

Table 7
Ablation experiment results.

Condition	Accuracy					
						Average
/	1	1	0.9792	0.9479	0.9792	0.9813
removing time shifting	0.8854	0.9286	0.9107	0.8642	0.9107	0.8999
removing envelope spectrum analysis	0.9688	0.9688	0.9732	0.9554	0.9554	0.9643
removing time shifting and envelope spectrum analysis	0.7679	0.7366	0.7589	0.7813	0.7455	0.758

specific steps and subsequently comparing the resulting outcomes. Consequently, the discussion focuses on three distinct conditions: removing time shifting, removing envelope spectrum analysis, and removing time shifting and envelope spectrum analysis. For samples that do not require frequency-domain transformation, the length d_1 is set to 1024 to ensure consistency in the data structure of the network. The accuracy results of ablation experiments using the CNN model are listed in Table 7. It reveals a strong correlation between prediction accuracy and processing procedure. Regardless of whether spectrum signals and time-series data, removing the time shifting step makes it challenging for the network to effectively extract fault components. In the case of the triboelectric signals studied here, which feature high output responses, eliminating the masking effect caused by the fundamental frequency is essential [7].

To demonstrate the applicability of the dataset, three classical machine learning architectures, including Decision Tree (DT), Random Forest (RF), and Support Vector Machine (SVM), are employed in the experiment. Three models are implemented with a standard configuration that has been widely recognized as effective and reliable [13], and are tuned to achieve their optimal performance to ensure a fair and meaningful comparison. The results of the confusion matrices of these models evaluated on their respective test sets are shown in Fig. 6(f). Only the DT model exhibits a slight confusion between inner race and cage fault states. Unlike the CNN, which is misled by the spectral features with uniform magnitude changes, the misclassification of DT may be ascribed to a close distribution of values between two fault states (as shown in Fig. 5(b) and (c)). This reflects the inherent limitation of a single-tree structure. Nevertheless, an average accuracy as high as 98.5 % still offers preliminary validation for the effectiveness of triboelectric signal features in fault diagnosis. With the interpretability of tree-based models retained, the RF model further improves classification accuracy and enhances stability, achieving full detection and correct classification of all fault states. SVM, suited for the case of high-dimensional data and small samples, also demonstrates a high diagnostic accuracy. For the robustness of the optimal models, the 5-fold cross validation is performed using the repeatedly divided training sets, and the results are listed in Table 8. In terms of empirical results, RF and SVM achieve higher accuracy and exhibit more stable performance compared to CNN. This is because the fault feature patterns have already been clearly extracted by the proposed method, allowing traditional machine learning models to directly utilize these features for precise classification. In contrast, CNN needs to relearn these features from limited samples, making it less efficient.

4.2. Comparison experiments on vibration signals data

For a comparison, a commercial vibration sensor (MMF KS96.100) as shown in Fig. 7(a) is installed on the bearing pedestal to collect vibration acceleration signals from the TE-bearing, with a sampling frequency of 2 kHz and a sampling time of 2 min. Fig. 7(b) shows the frequency spectra of the vibration acceleration signals at normal and fault states, spanning the frequency range of 0–500 Hz. Compare to the notable exception of a center frequency at 400 Hz caused by structural resonance, there is a low amplitude acceleration signal with the shaft rotational frequency f_s and its harmonics under the healthy condition and does not contain any distinct fault frequency components. In the faulty conditions, balls passing over a local defect on one bearing raceway generate pulses at one of the fundamental fault frequencies, either BPFO or BPFI. The local fault on the inner ring leads to a significant elevation in the BPFI and its harmonics in the frequency domain. Simultaneously, the amplitudes of BPFO and its harmonics also increase. As the sensor is mounted near the outer ring (as shown in Fig. 7(a)) and the vibration caused by the inner race defect propagates through the structure, the components related to BPFO may be present in the measured signal.

Then, the vibration signals are analyzed using the same learning models, each with their respective optimal hyperparameters. The results are shown in Fig. 7(c). The distinction of inner ring fault remains challenging, approximately 25 % of the samples are misdiagnosed by CNN and SVM. The misclassified results are more scattered in the DT model, showing it less effective in multi-class tasks with background noise. The RF demonstrates an outstanding performance on this issue, where the diagnostic accuracy is maintained above 98 %. Similarly, the models are repeatedly trained and tested five times to reduce randomness. The comparison of diagnostic accuracy over five rounds is illustrated in Fig. 7(d), together with the results of the current residual signals in Table 8. With the aid of the proposed embedded configuration and processing method, the average accuracy of the triboelectric current signals has reached the level comparable to the conventional vibration sensor. Specifically, in our case, the performance of triboelectric current outperforms that of vibration signals across several models. Moreover, in comparison to commercial vibration sensors, the in-situ monitoring measurement based on the triboelectric effect holds greater potential for

Table 8
Comparison of classification accuracies using machine learning methods.

No.	Accuracy (%)			
	CNN	DT	RF	SVM
0	1	0.97	1	1
1	1	0.985	1	1
2	0.9792	0.975	1	1
3	0.9479	0.985	1	1
4	0.9792	0.99	1	1
Average	0.9813	0.981	1	1

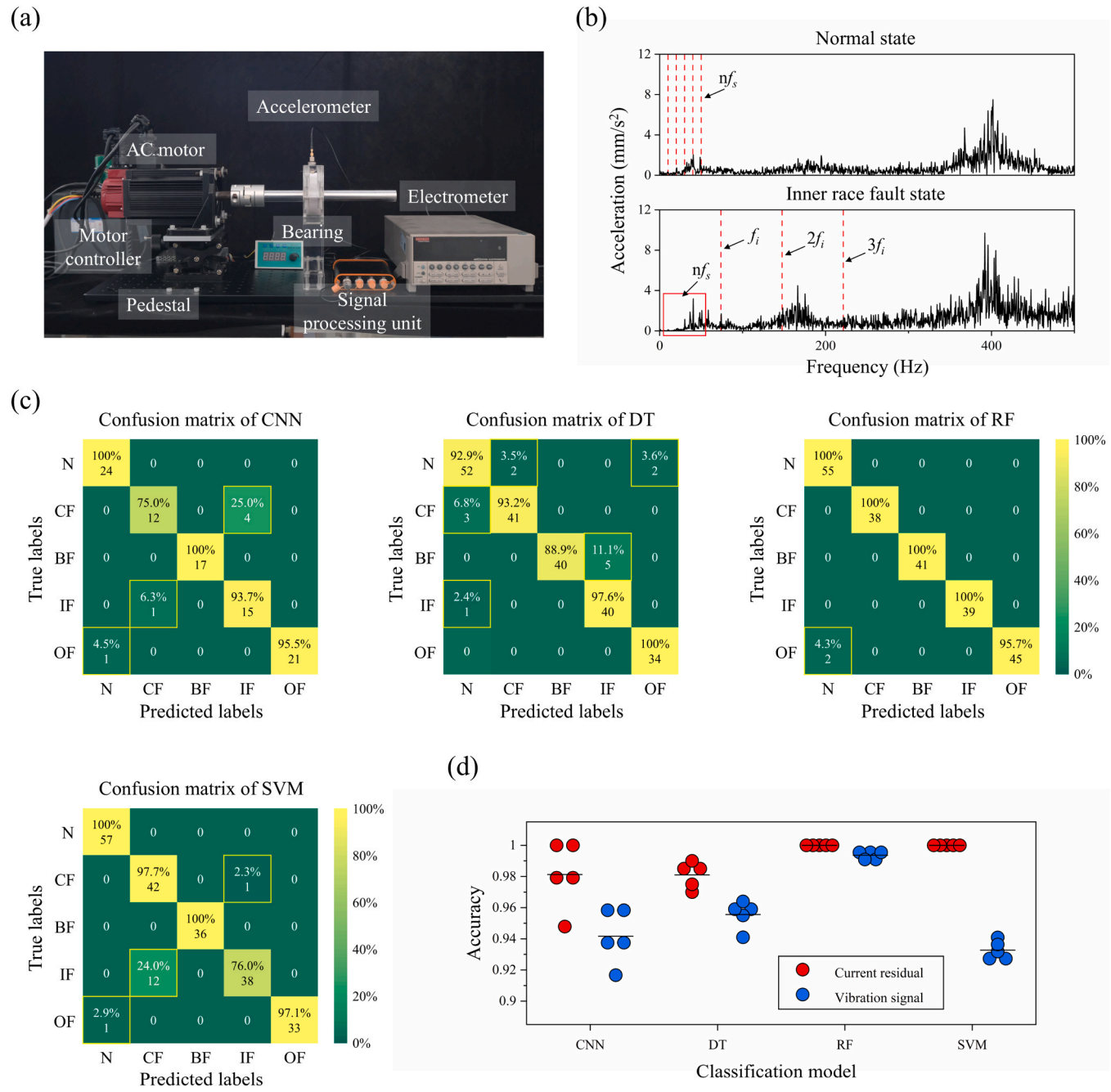

Fig. 7. Results of machine learning methods for Vibration acceleration Data. (a) Experimental platform for vibration signal acquisition. (b) Frequency-domain analysis results of vibration signals in normal and fault conditions. (c) Confusion matrices of four classification models: CNN, DT, RF and SVM. (d) Comparison of diagnostic performance using current residuals and vibration signals.

improvement [4]. These make it a promising solution to effectively mitigate the constraints associated with traditional sensor placement and complex transmission paths, as previously discussed.

4.3. Performance on time domain datasets

The advantages of deep neural network architectures are not fully manifested when processing frequency-domain data with clearly defined fault patterns. Of note, deep learning methods can adaptively extract fault features from raw signals, which eliminates depending on much prior knowledge about signal processing techniques and diagnostic expertise [32]. Here, five popular deep learning models for time-series data tasks, including CNN, CNN with Bidirectional Gated Recurrent Unit (CNN-BiGRU), Temporal Convolutional Network (TCN), Long Short-Term Memory Network with Attention Mechanism (LSTM-Atten), and Empirical Mode Decomposition and Transformer Network (EMD-Transformer), are employed to demonstrate the applicability of triboelectric signals in fault feature mining. Since the current residual signal is directly used in this experiment without manual feature extraction, the SW width is restored to $d_1 = 1024$, consistent with the input size used in previous models. The stride is defined as half of the window width, i.e., also 512, to ensure variation between samples while each sample contains enough current cycles for deeper feature extraction. Combining the segments from the five states, the input data is expected to (1120, 1024, 1) according to Eq. (19). And all hyperparameters have been tuned optimally. The penultimate layers of all

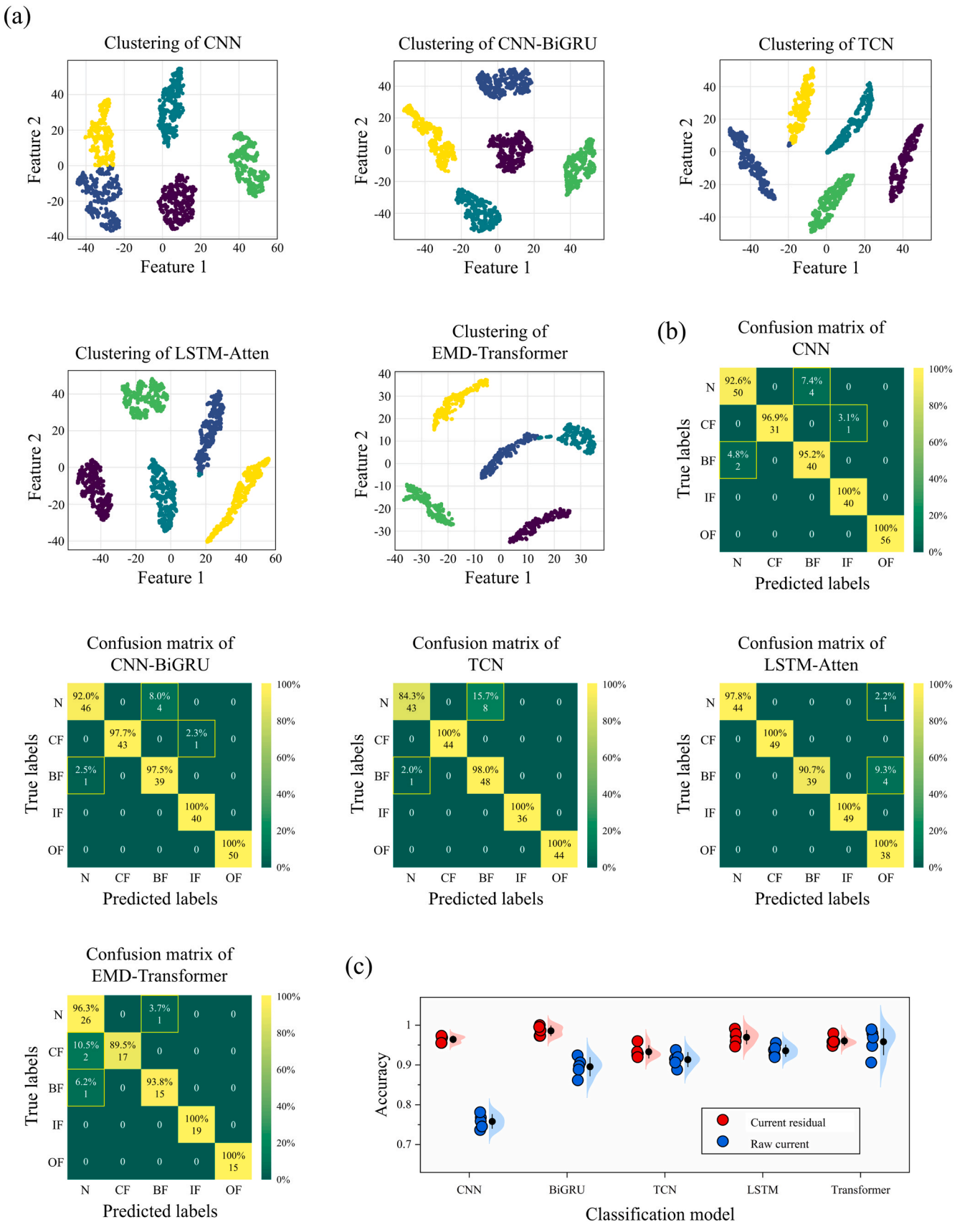

Fig. 8. Results of deep learning methods for Current residuals Data. (a) Feature visualization and (b) confusion matrices of five deep learning classification models: CNN, CNN-BiGRU, TCN, LSTM-Atten, and EMD-Transformer. (c) Comparison of diagnostic performance using current residuals and raw current signals.

models have been visualized in Fig. 8(a), providing an intuitive reading of the data distribution. All samples present a good clustering effect, highlighting that these representative deep learning models can effectively mine abstract features of different labels from the triboelectric dataset. Among them, CNN-BiGRU and LSTM-Atten demonstrate the least classification confusion, where the points of the same class are tightly clustered and clearly separated from other colors. This may be attributed to the enhanced temporal modeling capabilities of BiGRU and LSTM, which facilitate better recognition of the periodic patterns in triboelectric current signals. As shown in the confusion matrices of the final classification results (Fig. 8(b)), CNN-BiGRU and LSTM-Atten also achieve the most balanced performance corresponding to the t-SNE analysis, with over 97.5 % accuracy across most fault types. Most models present confusion between normal states and ball faults in this experiment. Specifically, TCN suffers from significant misclassification of 15.7 % of normal samples as ball fault states. As previously discussed, acting as a freestanding triboelectric layer, the motion of the surface-charged rolling elements generates the electrical signal. Local defect on one ball may not significantly disturb the collective motion of all balls, making such fault difficult to record, which often leads to similar signals. Our previous work provided a detailed analysis of this phenomenon and proposed an effective signal processing method suited for integration with CNN model [7]. Similarly, Fig. 8(c) visualizes the classification results from five rounds of repeated training and testing. Among them, four models achieve an average diagnostic accuracy of over 96 % on the current residual signals. When directly feeding raw current signals with similar waveforms into the network, the standalone CNN encounters significant challenges, with its accuracy dropping to 75.8 %. Fortunately, with the increasing complexity and representation capability, hybrid models combining sequential memory and attention mechanisms substantially mitigate the misclassification of raw signals.

4.4. Application in bearing self-powered condition monitoring

In addition to serving as a measurable signal for monitoring the bearing operation status, triboelectric technology, as a widely reported transduction method, has also been used to power some conventional electronics form rotational motion [4]. Here, the TE-bearing is employed to power an integrated wireless sensor node (WSN), demonstrating its superiority in both structural design and energy harvesting performance. Fig. 9(a) illustrates the experimental setup for the TE-bearing powering the WSN. The AC outputs generated by the TE-bearing are converted into DC through two full-bridge rectifiers. The energy management circuit integrating a buck converter, a storage capacitor of 47 μF, and a hysteresis comparator, is implemented based on the ViPSN YHL-A1 chip, with a complementary design to reduce energy consumption of the circuit and WSN [33]. The hysteresis comparator outputs operation instructions by comparing the capacitor voltage (>5 V or <3.5 V) to activate or sleep the circuit, thereby transferring energy to the signal transmission unit. Fig. 9(b) demonstrates the charging capabilities of the TE-bearing at 900 r/min for capacitors with varying capacitances. In the absence of external loads, commonly used capacitors of 10 μF, 47 μF, 100 μF, and 220 μF reaches the activation voltage of 5 V in approximately 16 s, 73 s, 119 s, and 279 s, respectively. Fig. 9(c) summarizes the charging times for the WSN under different rotational speeds. As the rotating speed increases, the storage capacitor charges more rapidly to 5 V, allowing the WSN to be activated more frequently. At 1200 r/min, only 56 s is required for charging. As shown in Fig. 9(d), the WSN successfully performs a real time monitoring of environmental temperature. Approximately 90 s after the bearing begins rotating, the collected information is wirelessly transmitted via Bluetooth and displayed on a mobile terminal, updating the real-time ambient temperature to 14.7 °C. Correspondingly, a demonstration video is provided in **Supplementary Movie S1**.

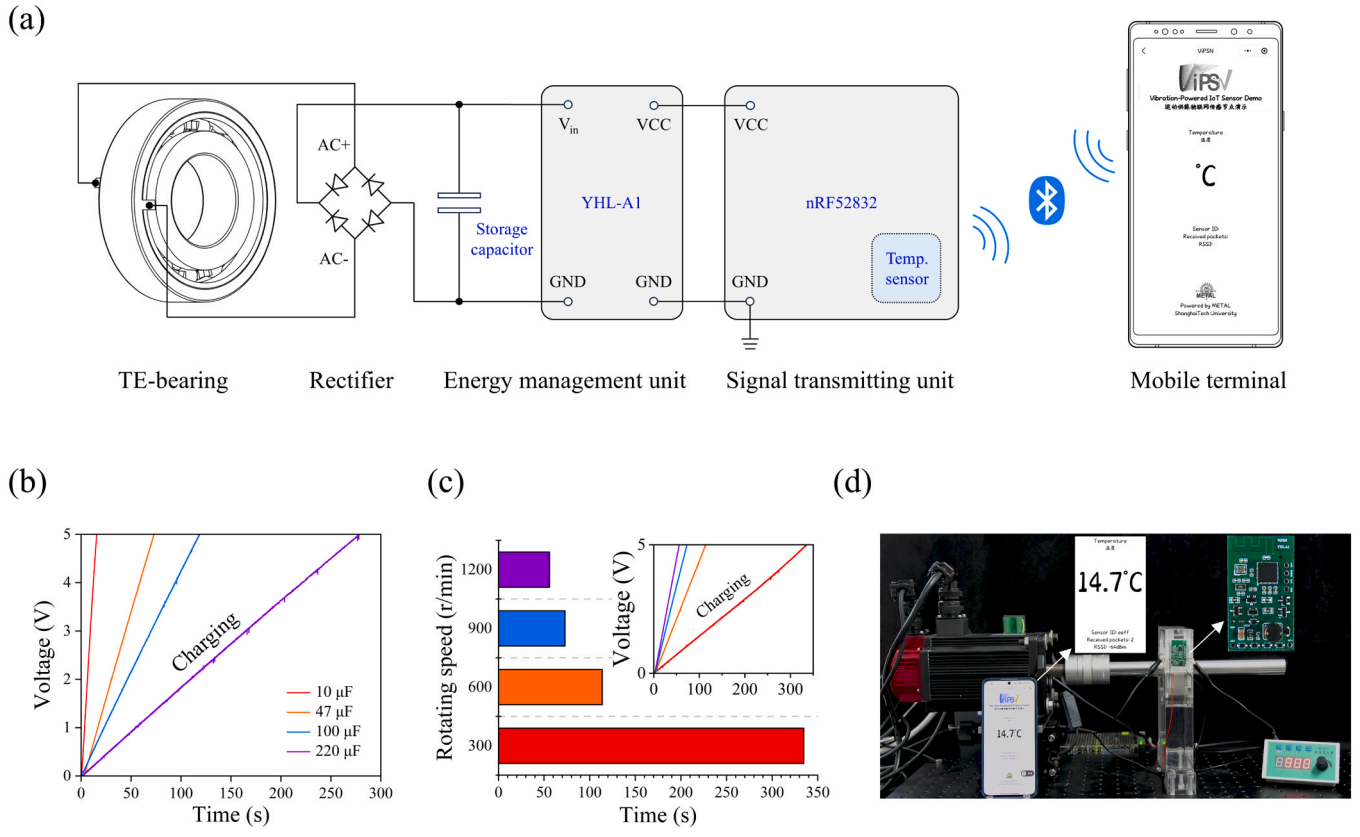

Fig. 9. Self-powering demonstration of the TE-bearing. (a) Circuit design and power management. (b) Charging curves of different capacitors at 900 r/min. (c) Charge capacity time with varying rotating speeds (of a 47 μF capacitor). (d) Photograph of the TE-bearing powering an integrated WSN.

Supplementary material related to this article can be found online at doi:10.1016/j.triboint.2025.111570.

If the self-powering capability of the TE-bearing can be further utilized to supply power for signal processing or wireless transmission of diagnostic results, the level of bearing intelligence would be significantly enhanced. At present, however, further exploration is still required in matching bearing materials, redesigning transduction structure, and optimizing energy management circuits in order to enhance the output performance of the TE-bearing. It is noteworthy that the current WSN can already be integrated onto a compact printed circuit board (PCB) of 36.5 mm× 21 mm in length and width, with a detailed view shown in the inset of Fig. 9(d). In the foreseeable future, such nodes could be mounted on flexible PCBs and fully embedded into the TE-bearing together with the electrodes, to form a self-powered smart bearing. For scenarios with compact layouts, the self-monitoring and self-powering based on the triboelectric effect present considerable opportunities for a new generation of smart bearings.

5. Conclusion

This paper develops an embedded triboelectric bearing for condition monitoring and local fault detection in rolling bearings. Interdigitated electrodes are embedded into the outer ring of a commercial bearing, enabling monitoring through triboelectrification between the rolling elements and raceways. Compared with common monitoring techniques, the triboelectric transducer provides electrical signals with more distinct fault features due to the shorter transmission path. Structural analysis confirms the mechanical feasibility of the embedded design under reasonable radial loads, and both FE modeling and experiments are performed to determine the optimal embedding depth and evaluate the electrical output. A processing methodology for triboelectric signals is proposed, where residual signals are extracted by time shifting to remove the fundamental component and highlight fault information. Experiments conducted on four faulty cases of cage, inner race, outer race, and rolling element, show that local faults induce impact features in the current signals, producing clear fault components in the envelope spectrum consistent with BCFs used in vibration-based diagnosis, enabling the estimation of fault location. The classification results using three classical machine learning algorithms validate the effectiveness of the extracted triboelectric signal features, achieving an average accuracy above 98 %. Comparative tests with a commercial accelerometer demonstrate the superiority of the embedded triboelectric transducer in frequency-domain analysis and diagnostic accuracy. Triboelectric signals also prove applicable to deep learning-based feature mining, where ablation experiments verify that the time shifting method significantly increases the accuracy of lightweight 1D-CNN models, reaching over 96 % across four popular models for time-series tasks. A fully self-powered bearing condition monitoring demonstration further shows the TE-bearing's practical potential, achieving wireless transmission and real-time temperature updates within 90 s at 900 r/min. Overall, this study represents a further step toward smart bearings with embedded triboelectric transducer. Future work will explore additional bearing types to support broader triboelectric-based smart bearing applications.

CRediT authorship contribution statement

Fangyang Dong: Writing – original draft, Visualization, Software, Project administration, Methodology, Investigation, Formal analysis, Data curation, Conceptualization. **Taili Du:** Writing – review & editing, Supervision, Project administration, Funding acquisition. **Minyi Xu:** Writing – review & editing, Supervision, Project administration, Funding acquisition. **Guang-An Yu:** Visualization, Software, Data curation. **Hengxu Du:** Visualization, Software, Data curation. **Peishuo Li:** Visualization, Software, Methodology, Investigation, Formal analysis, Data curation, Conceptualization. **Zhixiang Chen:** Visualization, Resources, Investigation, Data curation. **Zhiying Zhang:** Visualization, Resources. **Weilu Sha:** Visualization, Resources. **Yiyang Huo:** Visualization, Resources.

Declaration of Competing Interest

The authors declare that they have no known competing financial interests or personal relationships that could have appeared to influence the work reported in this paper.

Acknowledgements

The work is supported by the China Postdoctoral Science Foundation (Grant Nos. 2025T180074, 2024M750297), the Beijing Key Laboratory of High-Entropy Energy Materials and Devices, Beijing Institute of Nanoenergy and Nanosystems (Grant No. GS2025MS004), the Fundamental Research Funds for the Central Universities (Grant No. 3132025655), and Basic Research Project of the Liaoning Provincial Department of Education (LJ212510151019).

Appendix A

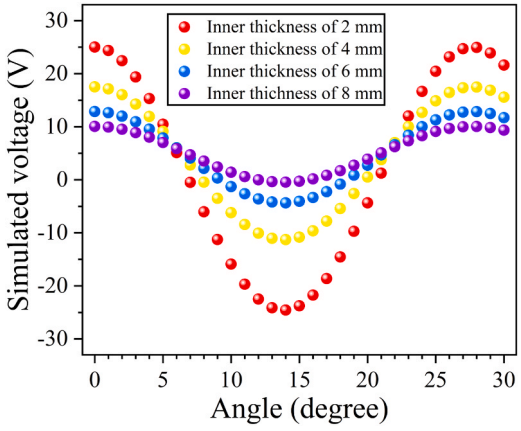

Fig. A.1. Variance of the simulated electric potential varies with the rotation angle of rolling elements

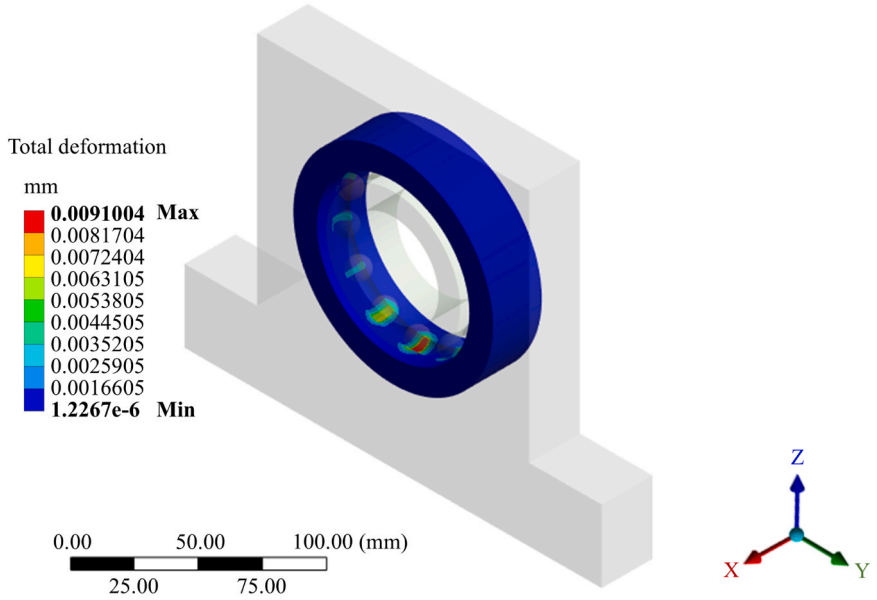

Fig. A.2. Deformation contour of the outer ring in the original bearing under a 1000 N radial load

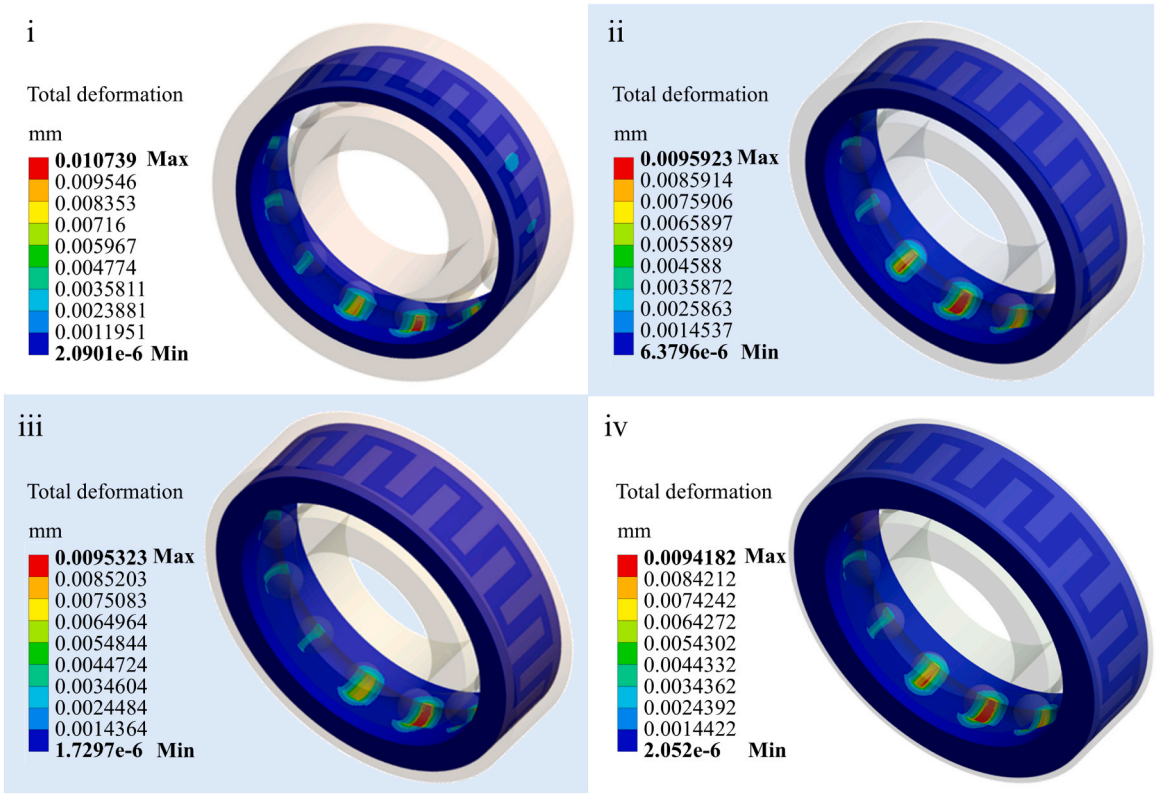

Fig. A.3. Deformation contour of inner shells under a 1000 N radial load (when the rolling element is located above the gap between comb fingers)

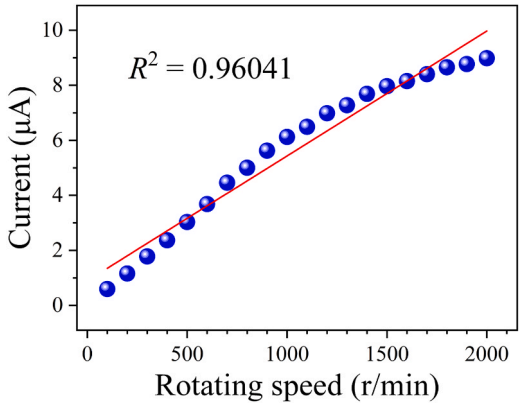

Fig. A.4. Relationship between the I_{SC} amplitude and the rotor speed

Data availability

Data will be made available on request.

References

[1] Zhu YS, Zhang P, Yuan QQ, Yan K, Hong J. Key technologies and development trend of smart bearing. J Vib Meas Diagn 2019;39:455–62.
[2] SKF Group. SKF launches SKF Insight™, groundbreaking intelligent bearing technology. 2013. ⟨https://www.skf.com/cn/news-and-events/news/2013/2013-Apr-08-skf-launches-skf-insight-groundbreaking-intelligent-bearing-technology⟩.
[3] Schaeffler Germany. Schaeffler VarioSense. 2019. ⟨https://www.schaeffler.de/en/news_media/media_library/downloadcenter-detail-page.jsp?id=87447361⟩.
[4] Zhang Y, Wang W, Wu X, Lei YG, Cao JY, Bowen C, et al. A comprehensive review on self-powered smart bearings. Renew Sust Energ Rev 2023;183:23.
[5] Zhang Y, Cao JY, Zhu HY, Lei YG. Design, modeling and experimental verification of circular Halbach electromagnetic energy harvesting from bearing motion. Energy Conv Manag 2019;180:811–21.
[6] Zhang LF, Zhang FB, Qin ZY, Han QK, Wang TY, Chu FL. Piezoelectric energy harvester for rolling bearings with capability of self-powered condition monitoring. Energy 2022;238:11.
[7] Dong FY, Zhu MX, Wang YL, Chen ZX, Dai YW, Xi ZY, et al. AI-enabled rolling triboelectric nanogenerator for bearing wear diagnosis aiming at digital twin application. Nano Energy 2025;134:13.
[8] Wang ZL. From contact electrification to triboelectric nanogenerators. Rep Prog Phys 2021;84:68.
[9] Han QK, Ding Z, Qin ZY, Wang TY, Xu XP, Chu FL. A triboelectric rolling ball bearing with self-powering and self-sensing capabilities. Nano Energy 2020;67:10.
[10] Dong FY, Yang HY, Du HX, Zhu MX, Xi ZY, Wang YL, et al. Triboelectric nanogenerator-embedded intelligent bearing with rolling ball defect diagnosis via signal decomposition and automated machine learning. Nano Energy 2024;119:12.
[11] Jiang ZY, Gao S, Kong Y, Pennacchi P, Chu FL, Han QK. Ultra-compact triboelectric bearing based on a ribbon cage with applications for fault diagnosis of rotating machinery. Nano Energy 2022;99:10.
[12] Gao S, Han QK, Zhang XN, Pennacchi P, Chu FL. Ultra-high-speed hybrid ceramic triboelectric bearing with real-time dynamic instability monitoring. Nano Energy 2022;103:13.
[13] Han QK, Jiang ZY, Xu XP, Ding Z, Chu FL. Self-powered fault diagnosis of rolling bearings based on triboelectric effect. Mech Syst Signal Proc 2022;166:14.
[14] Li XH, Han CB, Jiang T, Zhang C, Wang ZL. A ball-bearing structured triboelectric nanogenerator for nondestructive damage and rotating speed measurement. Nanotechnology 2016;27:9.
[15] Xie YN, Wang SH, Niu SM, Lin L, Jing QS, Yang J, et al. Grating-structured freestanding triboelectric-layer nanogenerator for harvesting mechanical energy at 85% total conversion efficiency. Adv Mater 2014;26:6599–607.
[16] Meng XS, Li HY, Zhu G, Wang ZL. Fully enclosed bearing-structured self-powered rotation sensor based on electrification at rolling interfaces for multi-tasking motion measurement. Nano Energy 2015;12:606–11.
[17] Safian A, Wu N, Liang XH. Development of an embedded piezoelectric transducer for bearing fault detection. Mech Syst Signal Proc 2023;188:21.
[18] Shi HT, Song ZT, Zhang A. Structure design and feasibility analysis of intelligent bearing with multi-parameter monitoring capability. Proc Inst Mech Eng Part CJ Eng Mech Eng Sci 2025;239:5092–106.
[19] Zhao HF, Wang H, Yu HY, Xu QH, Li XS, Guo J, et al. Theoretical modeling of contact-separation mode triboelectric nanogenerators from initial charge distribution. Energy Environ Sci 2024;17:2228–47.
[20] Niu SM, Liu Y, Chen XY, Wang SH, Zhou YS, Lin L, et al. Theory of freestanding triboelectric-layer-based nanogenerators. Nano Energy 2015;12:760–74.
[21] Niu SM, Liu Y, Wang SH, Lin L, Zhou YS, Hu YF, et al. Theory of sliding-mode triboelectric nanogenerators. Adv Mater 2013;25:6184–93.
[22] Zhang CL, Zhou LL, Cheng P, Yin X, Liu D, Li XY, et al. Surface charge density of triboelectric nanogenerators: Theoretical boundary and optimization methodology. Appl Mater Today 2020;18:8.
[23] Liu YK, Liu WL, Wang Z, He WC, Tang Q, Xi Y, et al. Quantifying contact status and the air-breakdown model of charge-excitation triboelectric nanogenerators to maximize charge density. Nat Commun 2020;11:8.
[24] El-Thalji I, Jantunen E. A summary of fault modelling and predictive health monitoring of rolling element bearings. Mech Syst Signal Proc 2015;60-61:252–72.
[25] Cerrada M, Sánchez RV, Li C, Pacheco F, Cabrera D, de Oliveira JV, et al. A review on data-driven fault severity assessment in rolling bearings. Mech Syst Signal Proc 2018;99:169–96.
[26] Smith WA, Randall RB. Rolling element bearing diagnostics using the Case Western Reserve University data: a benchmark study. Mech Syst Signal Proc 2015;64-65:100–31.
[27] Gao S, Han QK, Jiang ZY, Zhang XN, Pennacchi P, Chu FL. Triboelectric based high-precision self-powering cage skidding sensor and application on main bearing of jet engine. Nano Energy 2022;99:12.
[28] Guan BK, Bao XH, Qiu HT, Yang DL. Enhancing bearing fault diagnosis using motor current signals: A novel approach combining time shifting and CausalConvNets. Measurement 2024;226:14.
[29] Mohammed A, Djurovic S. Electric machine bearing health monitoring and ball fault detection by simultaneous thermo-mechanical fibre optic sensing. IEEE Trans Energy Convers 2021;36:71–80.
[30] Golafshan R, Sanliturk KY. SVD and Hankel matrix based de-noising approach for ball bearing fault detection and its assessment using artificial faults. Mech Syst Signal Proc 2016;70-71:36–50.
[31] van der Maaten L, Hinton G. Visualizing data using t-SNE. J Mach Learn Res 2008;9:2579–605.
[32] Jia F, Lei YG, Lin J, Zhou X, Lu N. Deep neural networks: a promising tool for fault characteristic mining and intelligent diagnosis of rotating machinery with massive data. Mech Syst Signal Proc 2016;72-73:303–15.
[33] Dong LW, Hu GB, Tang Q, Zhao CY, Yang F, Yang YW. Advanced aerodynamics-driven energy harvesting leveraging galloping-flutter synergy. Adv Funct Mater 2025;35:14.